Low-temperature Thermochronology of the Beartooth Conglomerate

A Thesis

Presented to

---

the Faculty of the Department of Geosciences

University of Houston

In Partial Fulfillment

of the Requirements for the Degree

Master of Science

By

David Koenig

May 2015

Low-temperature Thermochronology of the Beartooth Conglomerate

David Edward Koenig

APPROVED:

Dr. Peter Copeland, Chairman

Dr. Michael Murphy

Dr. William Meurer
ExxonMobil Corporation

Dean, College of Natural Sciences and Mathematics

Acknowledgements

First, a thank you to the University of Houston Geoscience faculty and staff. Being part of such an outstanding program for both undergraduate and graduate studies was both a source of fulfillment and great pride as I navigated the path to higher education. To Dr. Peter Reiners and his staff at the University of Arizona for the expeditious sample analysis that made this study possible. To my family for their support and encouragement over the years, especially my wife Karli. Without whom I may not have persevered. To Dr. Michael Murphy, whose influence inspired the love of fieldwork I'll carry for the rest of my life. Most importantly, to Dr. Peter Copeland who is solely responsible for my pursuit of a degree in geology. Pete, without you I would have gone off and done something foolish, like become a lawyer. I thank you all.

Low-temperature Thermochronology of the Beartooth Conglomerate

---

An Abstract of a Thesis

Presented to

the Faculty of the Department of Geosciences

University of Houston

In Partial Fulfillment

of the Requirements for the Degree

Master of Science

By

David Koenig

May 2015

ABSTRACT:

During the Laramide Orogeny, the crystalline core of the Beartooth Plateau in northwest Wyoming and south-central Montana was thrust over Mesozoic and Paleozoic rock in the adjacent Big Horn Basin. Omar et al. (1994) reported apatite fission-track data of 30 samples from ~4 km of vertical section through the Red Lodge corner of the Beartooth overthrust. These authors presented two hypotheses to explain these data, both of which describe rapid uplift in the Paleocene with a second uplift event during the late Miocene or early Pliocene. The period between these two uplift events was characterized by Oligocene and Miocene sedimentation (Hypothesis A), or by tectonic quiescence (Hypothesis B). In an attempt to test the hypotheses of Omar et al. (1994), apatites and zircons from Precambrian crystalline clasts within the synorogenic Beartooth Conglomerate were analyzed by (U-Th)/He methods. In all, 25 apatite and 15 zircon aliquots from 5 basement clasts were measured. Two clasts presented average zircon ages older than average apatite ages, which I interpret to be the result of natural radiation damage (raising the closure temperature of apatite and lowering the closure temperature of zircon), the possible presence of zircons with uranium-rich rims, or zircon inclusions within apatite grains. Two apatite aliquots gave ages younger than the depositional age of the conglomerate (~55 Ma), suggesting low helium closure temperatures or an incorrect assessment of the age of deposition. All remaining apatite apparent ages (~60 Ma to ~190 Ma) and zircon apparent ages (~100 Ma to ~800 Ma) suggest a period throughout the Phanerozoic characterized by slow burial since Cambrian exposure, which continued until rapid uplift initiation of the Beartooth Range (~60 Ma).

CONTENTS

FIGURES

FIGURES

TABLES

1. Introduction

A shift from normal high-angle subduction to flat slab subduction of the Farallon plate beneath the North American plate along the west coast of North America caused thick-skinned, basement-involved shortening throughout the Rocky Mountains of Colorado, Wyoming, and Montana (Dickinson and Snyder, 1976; Coney and Reynolds, 1977; Bird, 1998; Saleeby, 2003; DeCelles et al., 2004). Today, these basement block uplifts, which formed from late Cretaceous to Eocene time, remain prominent features of the Rocky Mountain foreland extending up to 1000 km inland of the active margin (Foose et al., 1961; Figure 1). The Beartooth Range of northwest Wyoming and south-central Montana is one of three major crystalline-cored uplifts flanking the Bighorn Basin that rose from the Cretaceous foreland basin of the western United States during the Laramide Orogeny (Figure 1). This ~80 by 40 km elevated crustal block of Precambrian crystalline basement trending northwest is nearly devoid of ~3-4 km of Paleozoic and Mesozoic sedimentary cover-rock present prior to uplift initiation (Foose et al., 1961). Uplift of the block during the Laramide Orogeny has generally been interpreted as the result of fault-propagation folding associated with movement along the 30-35° west-dipping Beartooth and Line Creek faults (Figure 2; Wise, 1983; Blackstone, 1986; DeCelles, 1991b;). It is likely that the Beartooth Range was not emplaced as a single thrusted block but rather was first deformed internally by folding and faulting (Wise, 1983; DeCelles 1991b). Wise (1983) suggests, for instance, that the anticlinal fold of Clarks Fork Canyon (Figure 2 and 10) in the eastern Beartooth Range may have been an early structure of the Bighorn Basin floor, later structurally reworked by the Beartooth Thrust, tilting it to its current position. Vertical displacement of the Red Lodge corner of

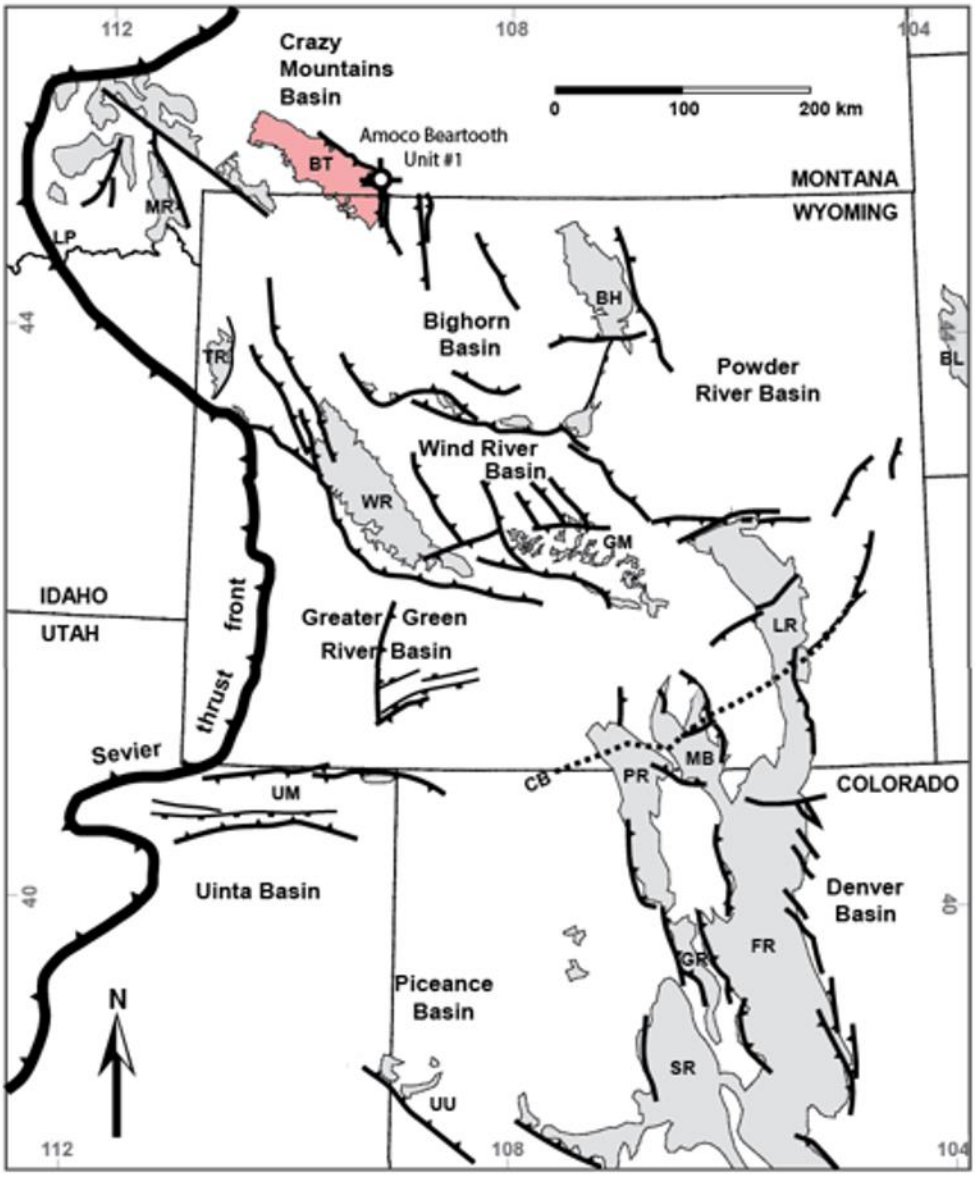

Figure 1: (modified from Peyton et al., 2012) Location map of Precambrian basement outcrop (gray shading), Precambrian basement outcrop of the Bearthooth Range (red shading) and major Laramide Rocky Mountain thrust faults. Abbreviations as follows: BL, Black Hills; BH, Bighorn Range; BT, Beartooth Range; CB, Cheyenne Belt; FR, Front Range; GM, Granite Mountains; GR, Gore Range; LP, Lima Peaks; LR, Laramie Range; MB, Medicine Bow Mountians; MR, Madison Range; PR, Park Range; SR, Sawatch Range; TR, Teton Range; UM, Uinta Mountains; UU, Uncompahgre Uplift; WR, Wind River Range.

the Beartooth Range associated with movement along the Beartooth and Line Creek thrusts has been estimated by regional cross-section of the Bighorn Basin constrained by well data (Blackstone, 1986), synorogenic conglomerate analysis (DeCelles, 1991b), and by thermochronological studies (Omar et al., 1994; Peyton et al., 2012) to be between ~6-12 km since early Paleocene time, placing Precambrian basement rock on top of Paleozoic and Mesozoic sedimentary rock of the adjacent Clark's Fork Basin (Foose et al., 1961; DeCelles et al., 1991b, Omar et al., 1994).

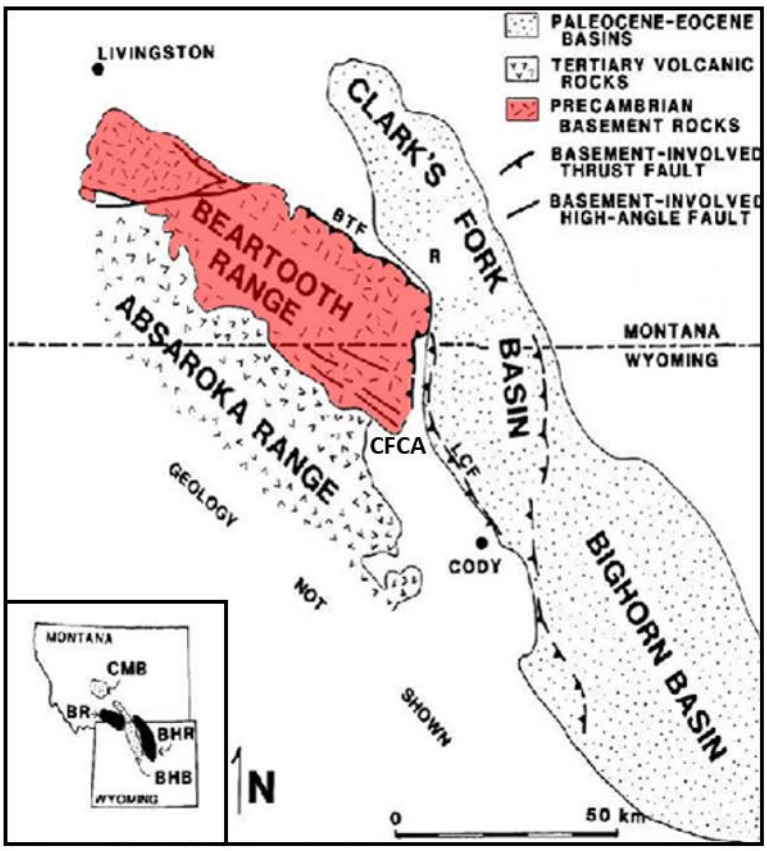

Figure 2: (modified from DeCelles et. al., 1991b) General map of south-central Montana and northwestern Wyoming showing locations of the Beartooth Range, Clark's Fork Basin, Bighorn Basin, Beartooth Fault (BTF) and Line Creek Fault (LCF). Map inset shows locations of the Beartooth Range (BR), Clark Fork Canyon Mouth Anticline (CFCA), Bighorn Range (BHR), Crazy Mountain Basin (CMB) and the Big Horn Basin (BHB).

Although the age of uplift initiation (early Paleocene) and early-Laramide kinematics of the Beartooth block are generally well agreed upon, less is understood about the timing and amount of post-Laramide uplift due to the absence of middle-Paleocene and younger rocks on the top of the Beartooth block as well as within the neighboring Bighorn Basin (Foose et al., 1961; DeCelles, 1991a). In this light it seems plausible the application of low-temperature thermochronometers on samples derived from the crystalline core of the Beartooth Range may have the potential to offer a better understanding of the timing of post-Laramide uplift and associated deformation.

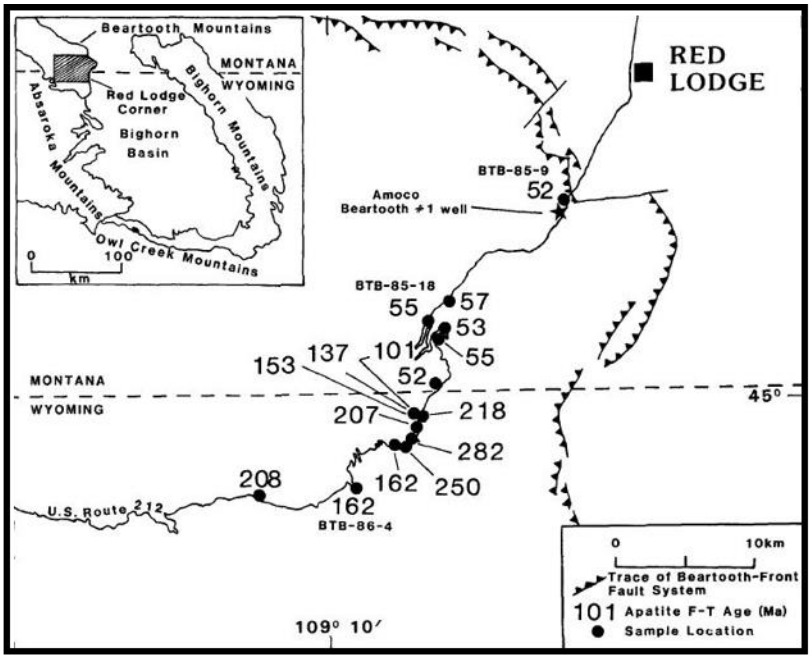

Figure 3: (modified from Omar et al., 1994) General map of south-central Montana and northwestern Wyoming showing sample location, location of Amoco Beartooth #1 well and Beartooth fault system.

1.1 **Apatite Fission-track Data**

Omar et al. (1994) reported results of apatite fission-track analyses (Figure 5) from samples collected from the southeast margin of the Beartooth Range (Figure 3). A fission-track is a narrow zone of deformation within a uranium-bearing grain that is caused by the movement of particles following the spontaneous fission of ^{238}U. Thus, fission-track density, the number of tracks per unit surface area, is a function of the apparent age of the grain and the concentration of ^{238}U (Naeser, 1979). An advantage of fission-track analysis is that it also provides valuable information about the grains temperature-time history (Omar et al., 1994). Omar et al. (1994) analyzed 26 samples from the upper plate of the Beartooth overthrust within the uplifted crystalline basement

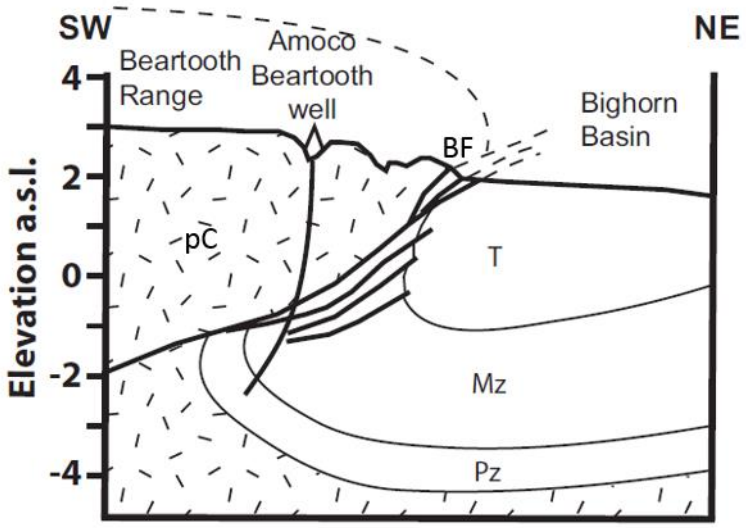

Figure 4: (modified from Peyton et al., 2012) Generalized cross-section of Beartooth Range and Bighorn Basin through Amoco Beartooth #1 well. Also shown are the Beartooth Fault (BF), Tertiary rocks (T), Mesozoic rocks (Mz), Paleozoic rocks (Pz) and Precambrian crystalline basement (pC).

block; 16 of which were collected from exposure along U.S. Route 212 south of Red Lodge, Montana and 10 from the subsurface acquired from the Amoco Beartooth #1 well (Figures 3 and 4) drilled 7 km south of Red Lodge, Montana (Omar et al., 1994). The suite of samples also included 1 sample from the shear zone and 3 sedimentary rock samples from the lower plate (footwall).

These 30 samples span 4 km of vertical section through the structure of the Red Lodge corner of the Beartooth Plateau (Omar et al., 1994). Apatite fission-track data from the samples (Figure 5) fell into two distinct groups based upon apparent age and mean fission-track length. The authors conclude from these data that the Red Lodge corner of the Beartooth overthrust was rapidly uplifted by 4-8 km during the late

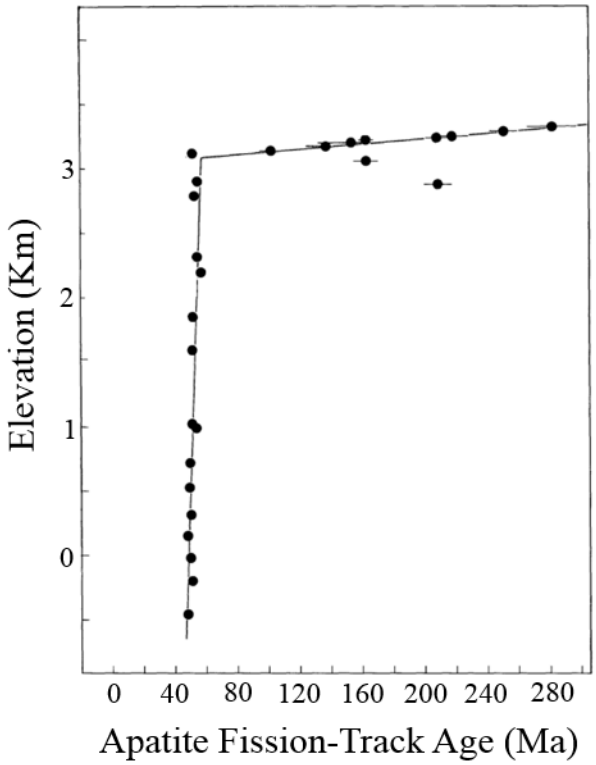

Figure 5: (modified from Omar et al., 1994) Apatite Fission-track age vs. present elevation for upper plate samples.

Paleocene as well as a subsequent late Miocene-early Pliocene (15 – 5 Ma) ~4 km uplift event responsible for the present day topographic relief of the Beartooth Plateau.

Omar et al. (1994) present two hypotheses that explain the apparent two-stage uplift interpreted from their data. Figure 6 illustrates the initial condition of both hypotheses based on the following geologic constraints: (1) The upper and lower boundaries of the fission-track partial-annealing zone are ~70 and ~125°C respectively. (2) The point of break in slope was ~6.8 km (~125°C) below sea level prior to the Laramide uplift event. (3) By the end of the Laramide event (early Eocene), the Beartooth block was ~600-800 m a.s.l. (4) Immediately before the second stage of uplift, the lowest three samples in the well were between 80 and 90°C.

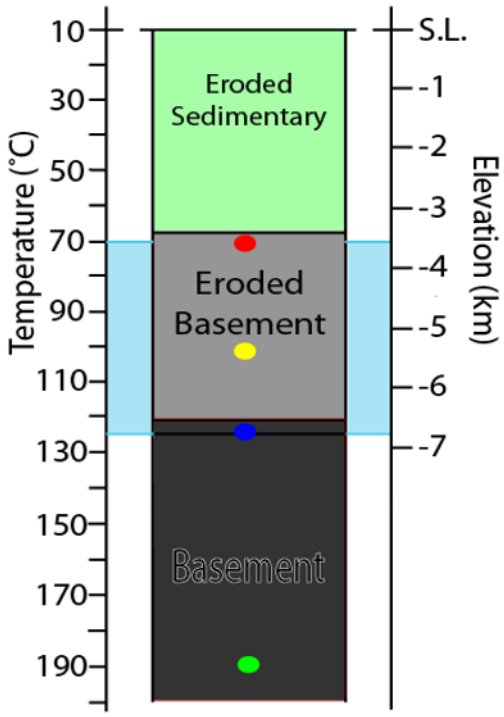

Figure 6: Omar et al., (1994) proposed position of samples from (A) the bottom of the well, (B) the break in slope, (C) and (D) two hypothetical samples within presently eroded Basement.

Hypothesis A: (Figure 7) After the first episode of uplift ended (early Eocene time), the lowest three samples from the upper plate were between 65 and 73°C. In order for these samples to have been between 80 and 90°C before the onset of the second period of uplift (15 – 5 Ma), this hypothesis suggests burial by 1-2 km of Oligocene or Miocene sediment.

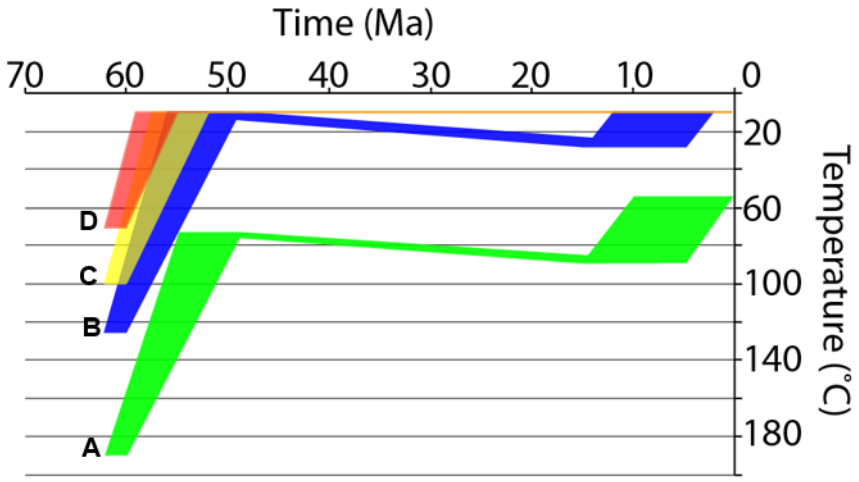

Figure 7: Time vs. Temperature plot representing Hypothesis A. (A) Lowest samples at ~190°C before Laramide uplift initiation and between 65ºC and 73°C by early Eocene time. (B) Samples just below the break in slope at ~125°C before Laramide uplift initiation. 1-2 km of burial during Oligocene and Miocene time putting the lowest samples between 80 and 90°C before the onset of the second period of uplift (15-5 Ma). (C) and (D) Temperature time paths of two hypothetical samples beginning at 70ºC and 100°C and eroded by end of first uplift episode.

Hypothesis B: (Figure 8) Here no mid-Cenozoic sedimentation is required but rather a period of tectonic quiescence. If cooling slowed or stopped after the first episode of rapid uplift while the samples at or near the break in slope were at temperatures <70°C

then samples near the bottom of the section would have stalled within the partial annealing zone at temperatures between 80-90°C for adequate time before the onset of the Miocene – early Pliocene uplift event to produce the observed fission-track data.

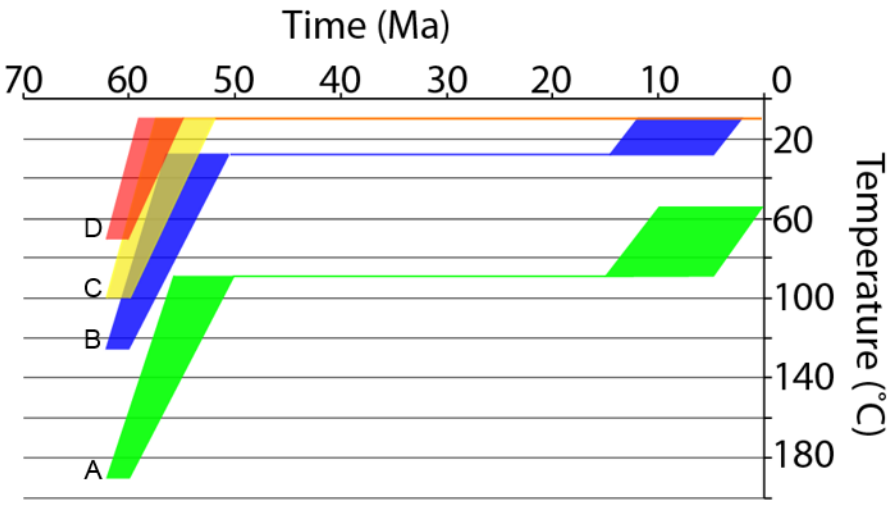

Figure 8: Time vs. Temperature plot representing Hypothesis B. (A) Lowest samples at 190°C before Laramide uplift initiation and between 80ºC and 90°C by early Eocene time. (B) Samples just below the break in slope at 125°C before Laramide uplift initiation. Tectonic quiescence during Oligocene and Miocene time. Uplift resumed between 15 and 5 Ma. (C) and (D) Temperature time paths of two hypothetical samples beginning at 70ºC and 100°C and eroded by end of first uplift episode.

1.2 Apatite (U-Th)/He Data

Over the past two decades the application of (U-Th)/He thermochronometry to better understand the timing and extent of regional deformational processes has increased as apatite helium diffusion has become better understood. (Shuster and Farley, 2003; Shuster et al., 2006; Flowers et al., 2009; Spiegel et al., 2009) With an average closure temperature of ~75ºC, the apatite-He system has, potentially, the ability to better

understand that which occurs within the uppermost 1-3 km of the Earth's surface (Wolf et al., 1996). Peyton et al., (2012), as part of a larger synthesis study of the low-temperature history of the Laramide ranges, reported apatite-He ages from 24 samples (Figure 9) collected both from the surface and subsurface of the Beartooth Range which resembles the sample suite measured by Omar et al., (1994). From the data obtained in Peyton et al., (2012) the authors suggest that the onset of rapid uplift of the Red Lodge corner of the Beartooth Range began no later than ~58 Ma. While the trend in ages broadly approximates results of Omar et al. (1994), Peyton et al. (2012) report the data cannot be interpreted to better understand the timing and extent of post-Laramide deformation.

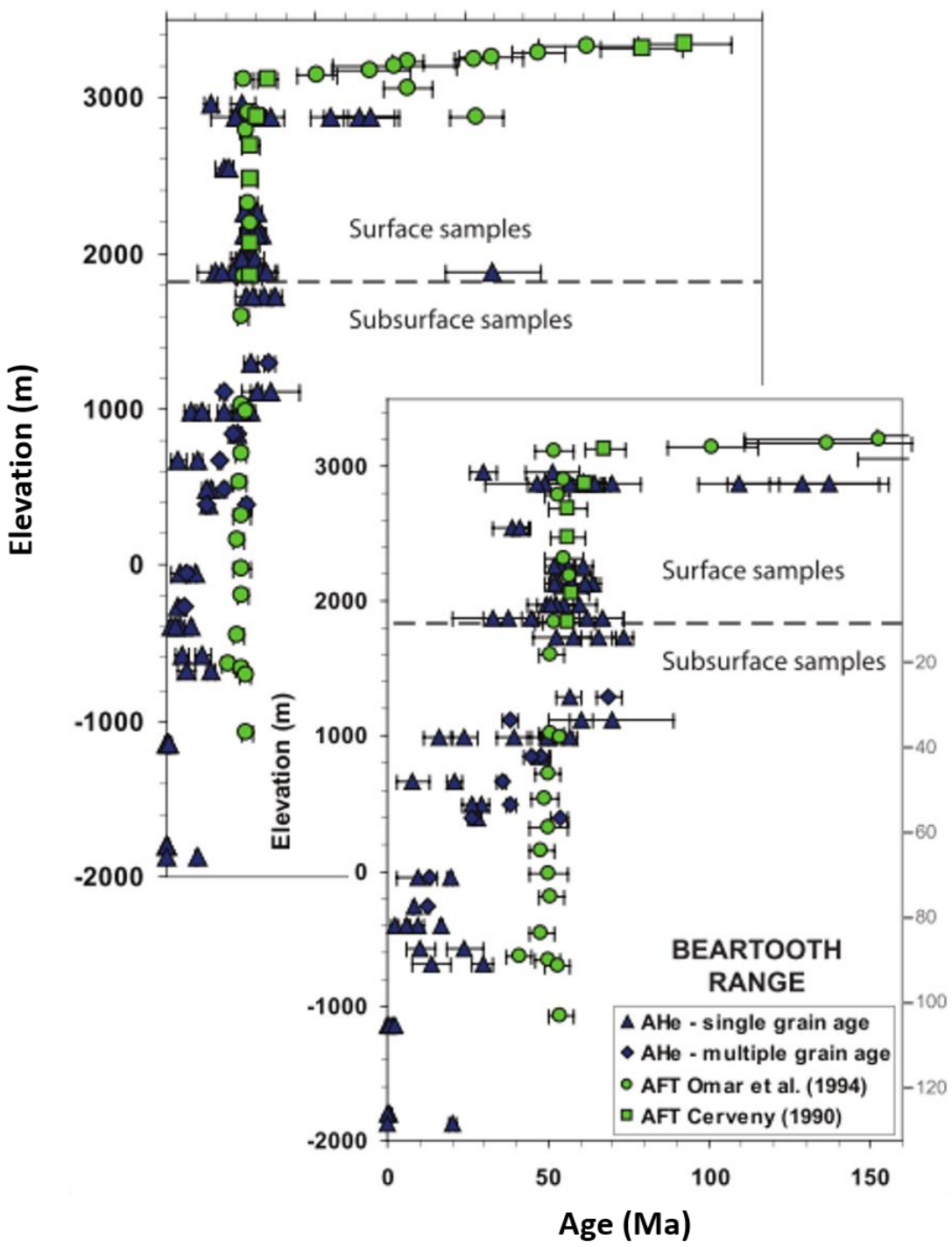

Figure 9: (modified from Peyton et al., 2012) AHe and AFT ages from the Beartooth Range as a function of elevation. As well as AHe data from the study (dark blue triangles) the authors included AFT data from Omar and others (1994) (green circles) and Cerveny (ms, 1990) (green squares). Dashed line represents surface elevation. All error bars are 2σ.

1.3 (U-Th)/He Data from Crystalline Conglomerate Clasts

To date, thermochronogical studies of the basement-cored uplifts of the Laramide province have been applied to surface and subsurface samples in-place within the ranges. Because many of these ranges are flanked by synorogenic conglomerates rich in range derived crystalline basement clasts, it seems reasonable that a low-temperature thermochronological investigation of grains within these clasts may offer tests of the post-Laramide hypotheses proposed by Omar et al., (1994). This study applies the (U-Th)/He thermochronometer to apatite and zircon grains from clasts harvested from within the Beartooth Conglomerate (Figure 10 and 11) with the goal of testing the two hypotheses of Omar et al. (1994).

Informally defined by DeCelles (1991a; Figures 10 and 11) as the belt of coarse, Upper-Paleocene conglomerate that extends around the perimeter of the Beartooth Range from Clark's Fork of the Yellowstone River in Wyoming to West Red Lodge Creek in Montana, the Beartooth Conglomerate was deposited in angular unconformity above Cretaceous rocks in the Bighorn Basin (DeCelles et al., 1991b). The Upper-Paleocene depositional age determination is widely agreed upon though the name and areal extent vary. Floral data reported by Hickey (1980) from within the Beartooth Conglomerate suggest a late Paleocene age and the unit is reported to interfinger with the rocks of the Fort Union Formation, thought to be late Paleocene based on floral and faunal fossil ages. These ages are consistent with Fleuckinger, (1972) and Jobling, (1974). Intra-formational structures indicative of growth strata and evidence of synorogenic deposition, including several angular unconformities, exist within the Beartooth Conglomerate, which formed

as proximal fan sedimentation rotated eastward as a result of uplift of the Beartooth Range. Each successive uplift stage caused basin-ward rotation and stepwise deposition of conglomeratic facies which lie in angular unconformity on top of one another (Dutcher et al., 1986; DeCelles et al., 1991b). Figure 10 shows the clast-type distribution within the Beartooth Conglomerate. Precambrian crystalline clasts are reported by DeCelles et al., (1991b) to be present within the facies between Bennett Creek and Line Creek (Figure 10).

Prior to processing the samples collected for this study, predicted apatite-He ages were obtained using HeFty modeling software (Ketchem, 2005) for samples that lie just below the break in slope described by Omar et al., (1994) (Figure 5) and samples at the

	Predicted Apatite Age	
Sample	**Hypothesis A**	**Hypothesis B**
(D) 70˚C	61-58 Ma	61-58 Ma
(C) 100˚C	61-58 Ma	61-58 Ma
(B) Break in slope	58-54 Ma	57-52 Ma
(A) Bottom of well	10-3 Ma	10-3 Ma

Table 1: Predicted apparent ages following temperature-time paths of hypotheses A and B of Omar et al. (1994).

bottom of the well for both suggested hypotheses and are summarized in Table 1.

Because the authors provide uncertain age ranges for the end of the Laramide event (early Eocene) and the onset of the second period of uplift (15 – 5 Ma), apparent

ages were modeled using both the upper and lower limits of given age ranges. In addition, two hypothetical samples were modeled initially residing at temperatures of 70 and 100°C before the onset of the Laramide Orogeny (Figures 6,7, 8, Table 1). Samples at hypothetical depths, according to the proposed hypotheses of Omar et al., (1994), would have been eroded and deposited in the adjacent basin by the end of the Laramide event. Thus, these predicted apatite apparent ages represent possible ages for crystalline clasts collected from the Beartooth Conglomerate.

Predicted apatite apparent ages from samples collected near the break in slope following the temperature-time path suggested by Hypothesis A range from 58.6 Ma and 54.2 Ma. Samples from the bottom of the well range between 10-2.9 Ma. Ages of samples from both 70 and 100°C range between 61 and 58 Ma, respectively. Modeled apatite-He ages following the temperature-time path of Hypothesis B range between 57.5 Ma and 52.6 Ma for samples near the break in slope and from 10 Ma to 3 Ma for samples at the bottom of the well. Again, as in Hypothesis A, samples beginning at temperatures of 70 and 100°C range between 61Ma and 58 Ma.

From these predictions some inferences can be made. For instance, if apatite apparent ages from the Beartooth Conglomerate are much older than ~61 Ma, it may suggest that the thickness of Paleozoic and Mesozoic sedimentary cover (~3.4 km) used in the two hypotheses of Omar et al. (1994) has been over estimated. On the other hand, if apatite-He ages from clasts within the Beartooth Conglomerate are much younger than ~58 Ma it would suggest, possibly, that erosion of the Beartooth Plateau and deposition of the Beartooth Conglomerate may have carried some time into the Eocene.

2. Sampling, Descriptions and Methods

With the motivation of contributing to the elucidation of post-Laramide deformation in the Beartooth Range with respect to the two hypotheses presented by Omar et al., (1994), six crystalline clasts (LC1-A through LC1-F) were collected from the

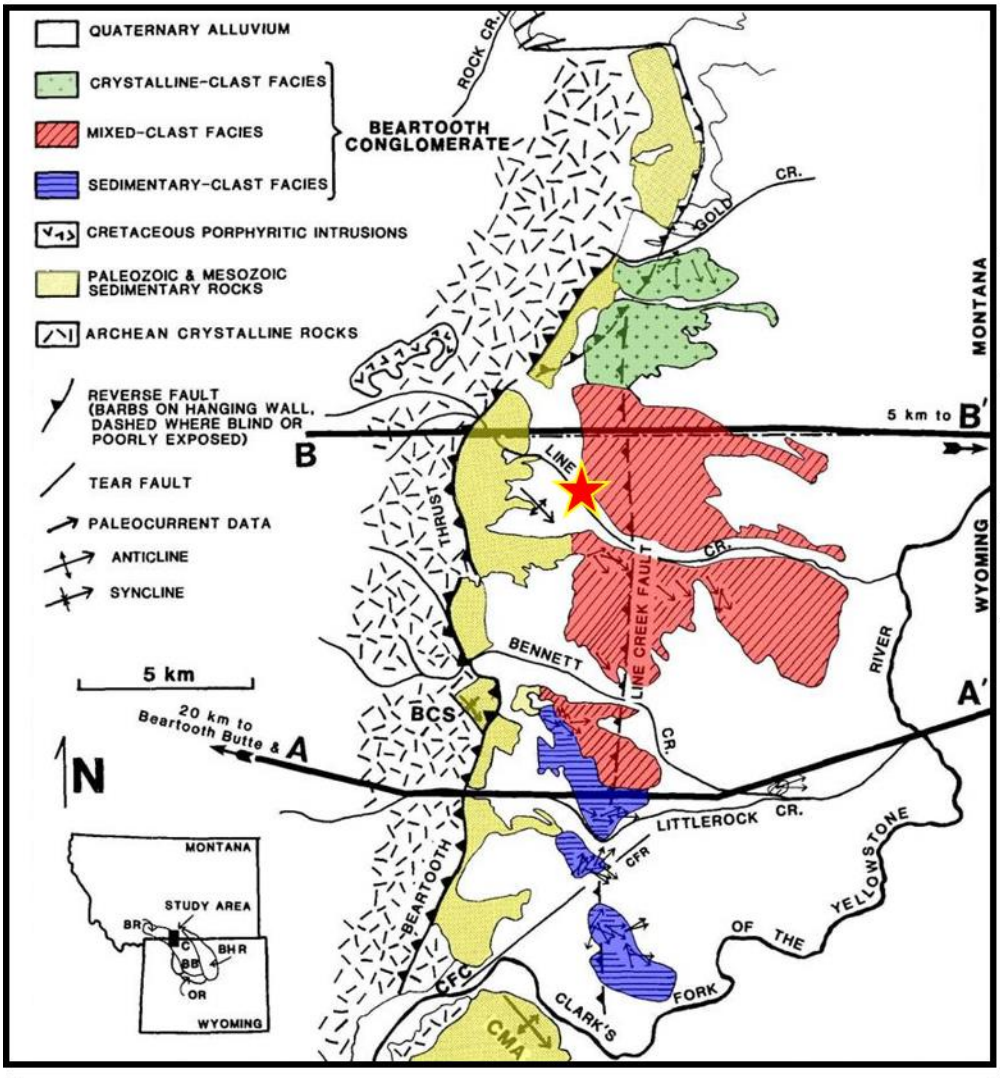

Figure 10: (modified from DeCelles et al., 1991b) Clast sample location (red star) Orientation and facies distribution of the Beartooth Conglomerate. Location of Clark's Fork Canyon anticline (CMA)

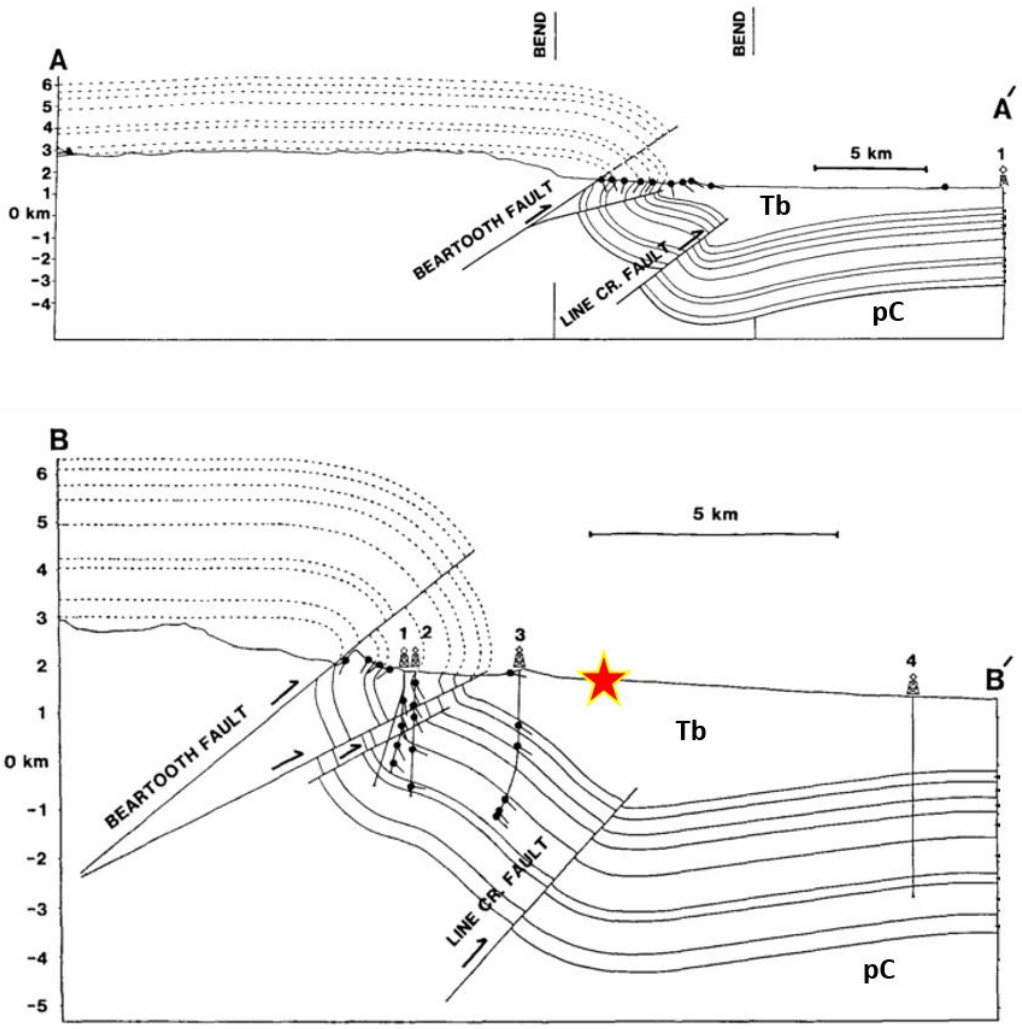

Figure 11: (modified from Decelles et al., 1991b) Cross sections A-A' and B-B' from figure 10. Sample location for this study is projected onto section B-B' (red star).

synorogenic Beartooth Conglomerate. All samples were harvested from a mixed-clast facies exposure along Line Creek described by DeCelles (1991a; Figure 10 and 11).

LC1-A (Figure 12) is a moderately weathered granite composed of quartz, potassium feldspar, plagioclase and biotite. Grain size averages around 3mm and the sample shows slight banding of clay minerals.

LC1-B (Figure 12) is a moderately weathered dark green diorite dominantly composed of anhedral amphibole and euhedral plagioclase feldspars occurring in equal proportions. The feldspar grains range in size from .1-2 cm and are randomly distributed throughout the sample with no preferred orientation. Alteration is common in the amphibole where oxidation has occurred.

LC1-C and **LC1-D** (Figure 13) are moderately weathered, well-foliated granitic gneiess containing quartz, potassium feldspar, plagioclase feldspar and biotite. Most grains are anhedral and range in size from <1mm to 2cm. Foliation is defined by clay minerals and feldspars.

LC1-E (Figure 14**)** is a moderately weathered, very well foliated granitic gneiss containing quartz, potassium feldspar, plagioclase feldspar and biotite. The sample is banded alternating between dark biotite rich and lighter feldspar and quartz-rich areas.

LC1-F (Figure 14) is a weathered, well-foliated garnet-bearing schist dominantly composed of amphibole, plagioclase and biotite which has been oxidized.

Each of the six clasts were crushed, washed and sieved to produce two separate grain-size aliquots motivated by **A)** the necessity of grains large enough to contain a measureable amount of radiogenic helium as well as minimize the role of α-ejection on helium age (Farley et al., 1996; Farley et al., 2002) and **B)** the possibility that suitable apatite and zircon grains would not be present in the largest grain-size fraction. The first aliquot was processed to contain grains 150-212 μm and the second (smaller fraction) 150-125 μm.

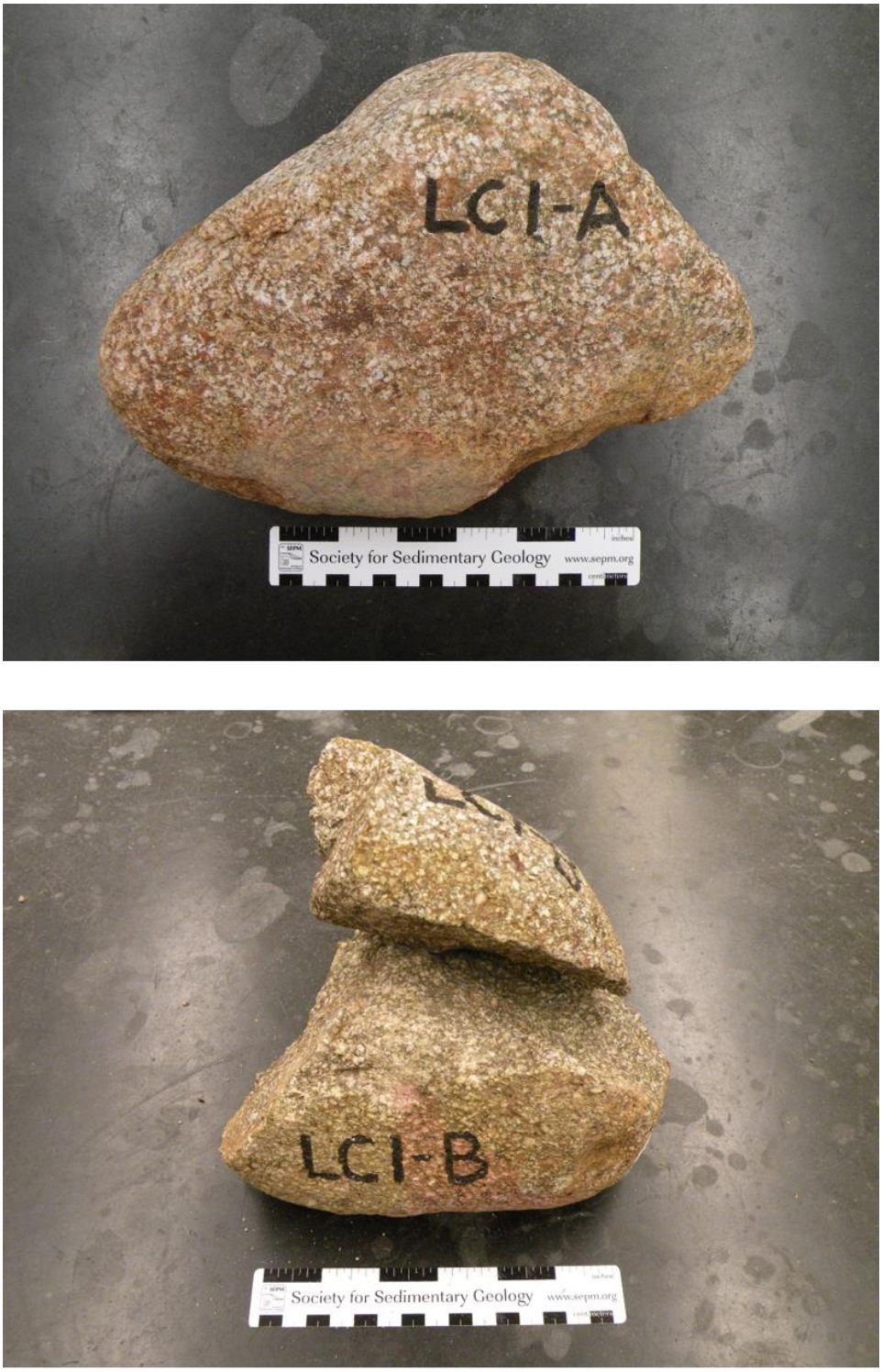

Figure 12: Photographs of samples LC1-A (Granite) and LC1-B (Diorite). Six inch scale.

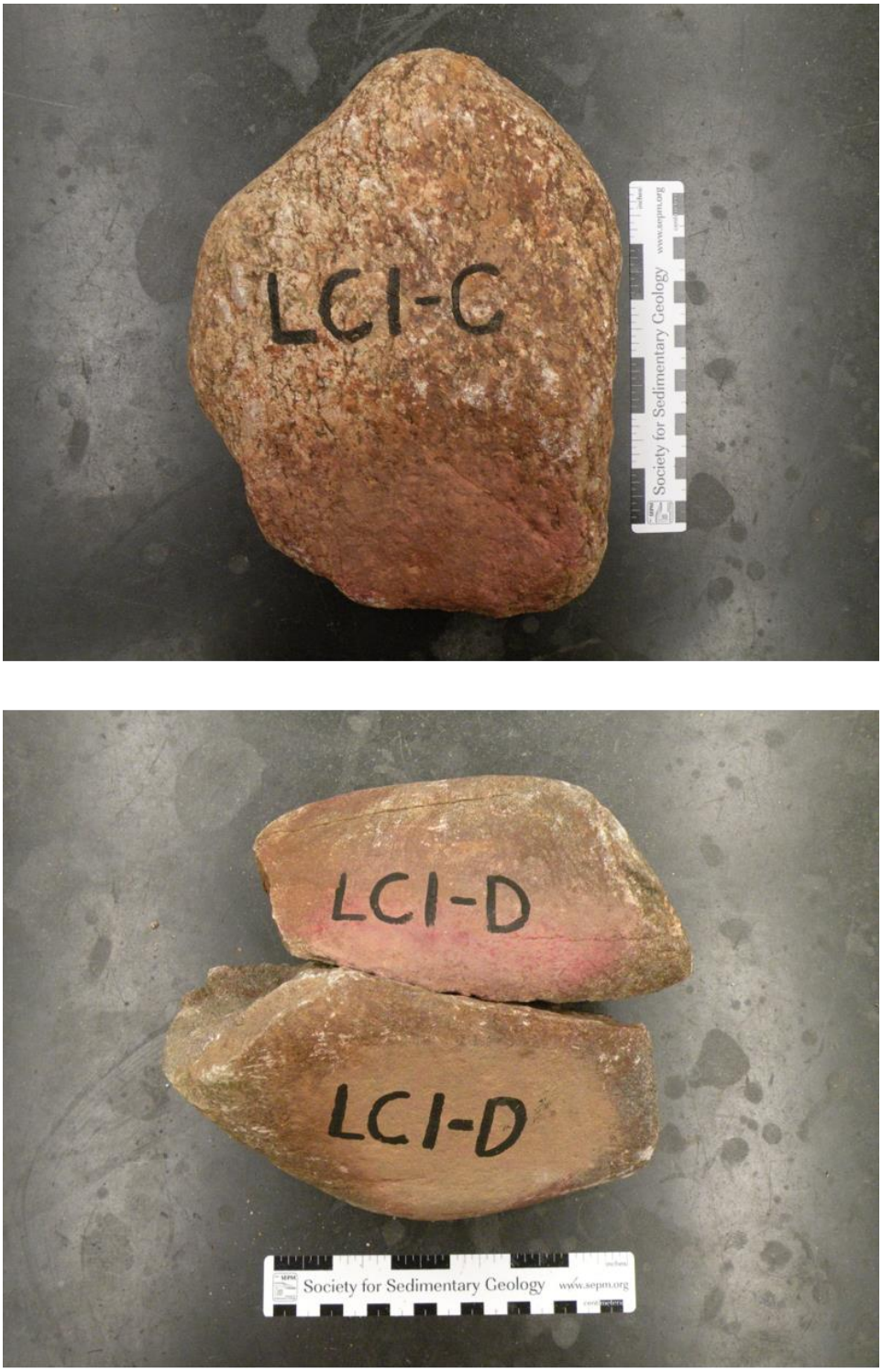

Figure 13: Photographs of samples LC1-C and LC1-D (Granitic gneiss). Six inch scale.

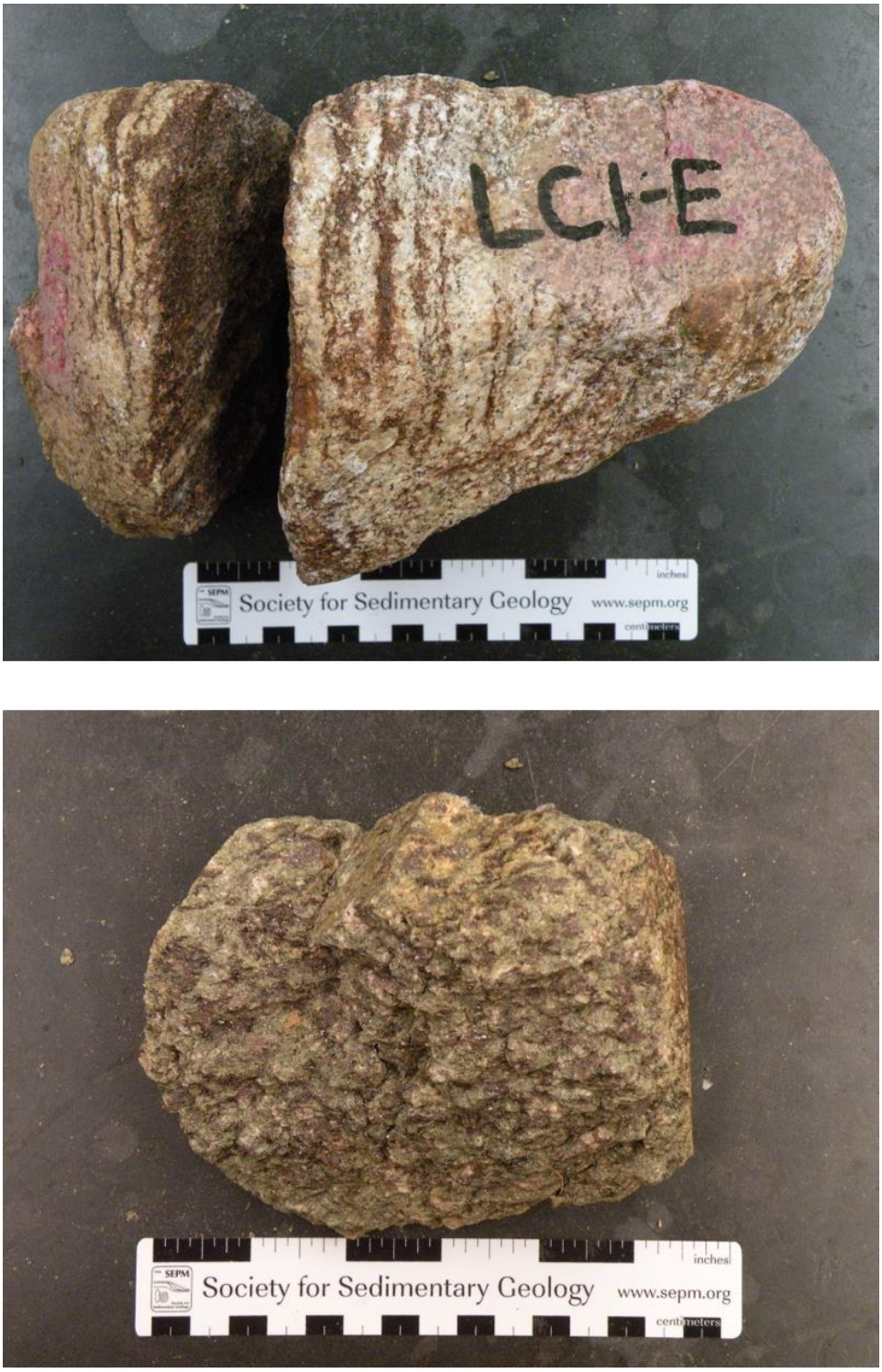

Figure 14: Photographs of samples LC1-E (Granitic gneiss) and LC1-F (Garnet bearing schist). Six inch scale.

Grains were then separated with bromoform to isolate minerals with densities >3.0 and again with methylene iodide to isolate minerals with densities >3.32, thus, separating apatite grains from zircon grains. Finally, each aliquot for the 6 samples was further separated by magnetic susceptibility. Apatite and zircon grains were selected via binocular petrographic microscopy based on crystal size, preservation of habit and absence of visible inclusions to mitigate the presence of parentless helium in apatite analyses and anomalously old apatite apparent ages (Vermeesch et al., 2006). Selected apatite and zircon grains were measured, photographed then packaged in Pt and Nd tubes, respectively. Radiogenic helium measurement was performed in the University of Houston Geochronology Laboratory using Nd:YAG laser heating and quadrupole mass-spectrometry (Copeland et al, 2007). Analyses were completed via isotope dilution and HR-ICP-MS at The University of Arizona following procedures described in Reiners et al. (2004). Raw ages were corrected for α-ejection in accordance with Farley et al., (2002). In total, 40 samples were prepared for analysis. Five apatite aliquots (two of which contained multiple grains, the remaining three were single grain aliquots) were analyzed from cobbles LC1-B, LC1-C, LC1-D, LC1-E, and LC1-F and three single crystal zircon aliquots from LC1-B, LC1-C, LC1-E, and LC1-F. Photographs of all analyzed grains are shown in Figures 15-19.

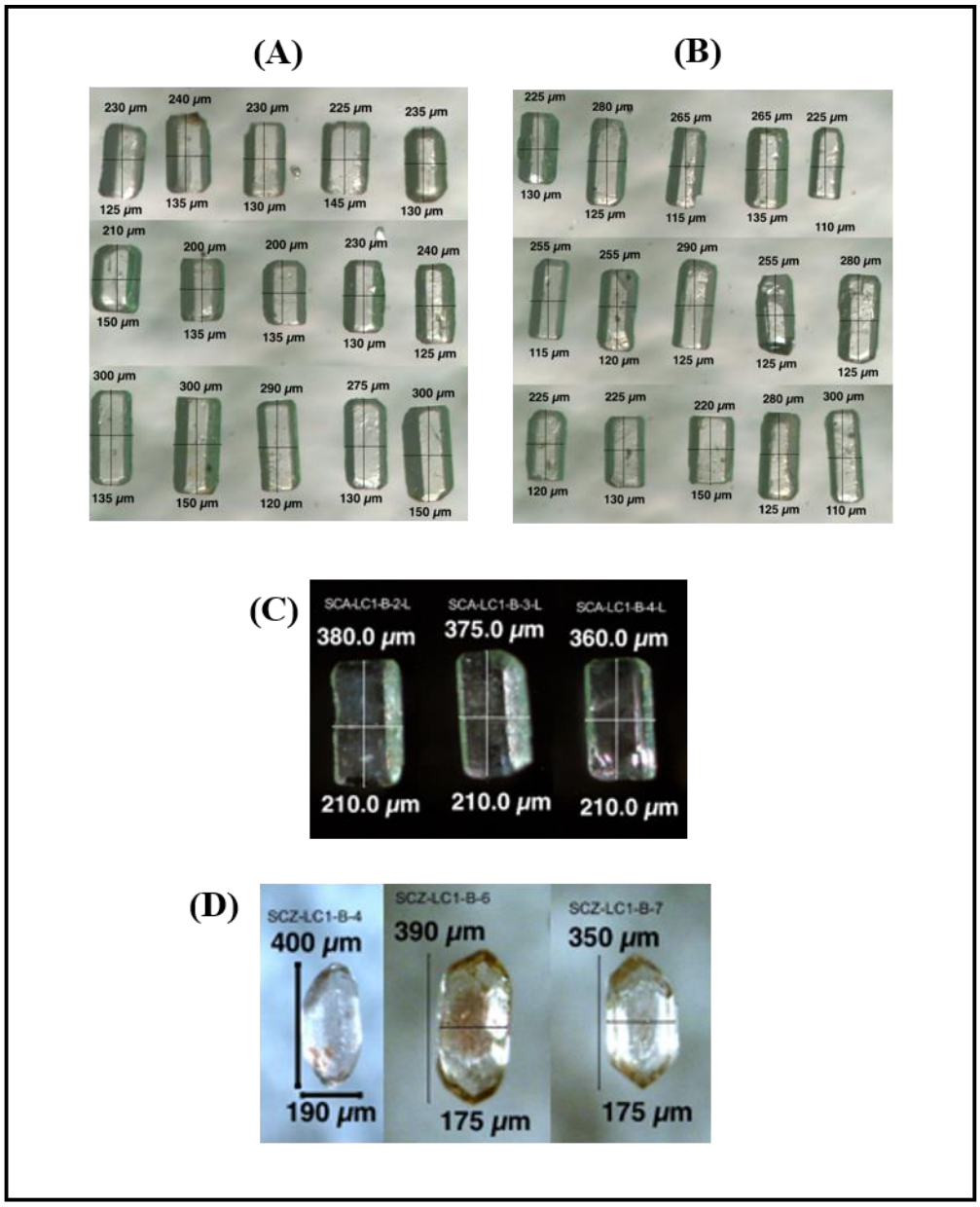

Figure 15: Clast LC1-B (diorite) analyzed grains, (A) MCA-LC1-B1-3 apatite. (B) MCA-LC1-B4-6 apatite. (C) Single grain apatite aliquots: SCA-LC1-B-2, SCA-LC1-B-3, SCA-LC1-B-4 (D) Single grain zircon aliquots: SCZ-LC1-B-4, SCZ-LC1-B-6, SCZ-LC1-B-7.

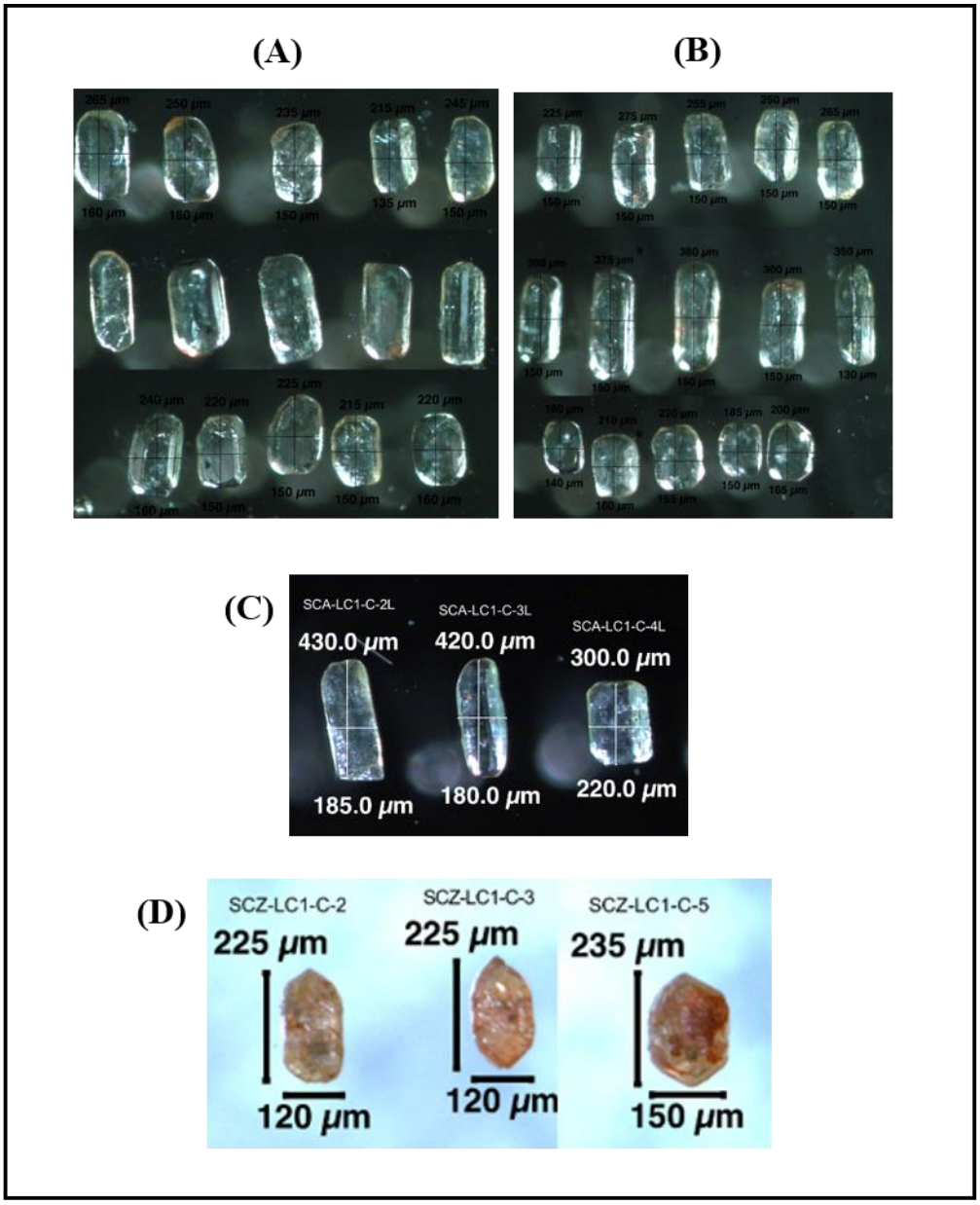

Figure 16: Clast LC1-C (granitic gniess) analyzed grains, (A) MCA-LC1-C1-3 apatite. (B) MCA-LC1-C4-6 apatite. (C) Single grain apatite aliquots: SCA-LC1-C-2, SCA-LC1-C-3, SCA-LC1-C-4 (D) Single grain zircon aliquots: SCZ-LC1-C-2, SCZ-LC1-C-3, SCZ-LC1-C-5.

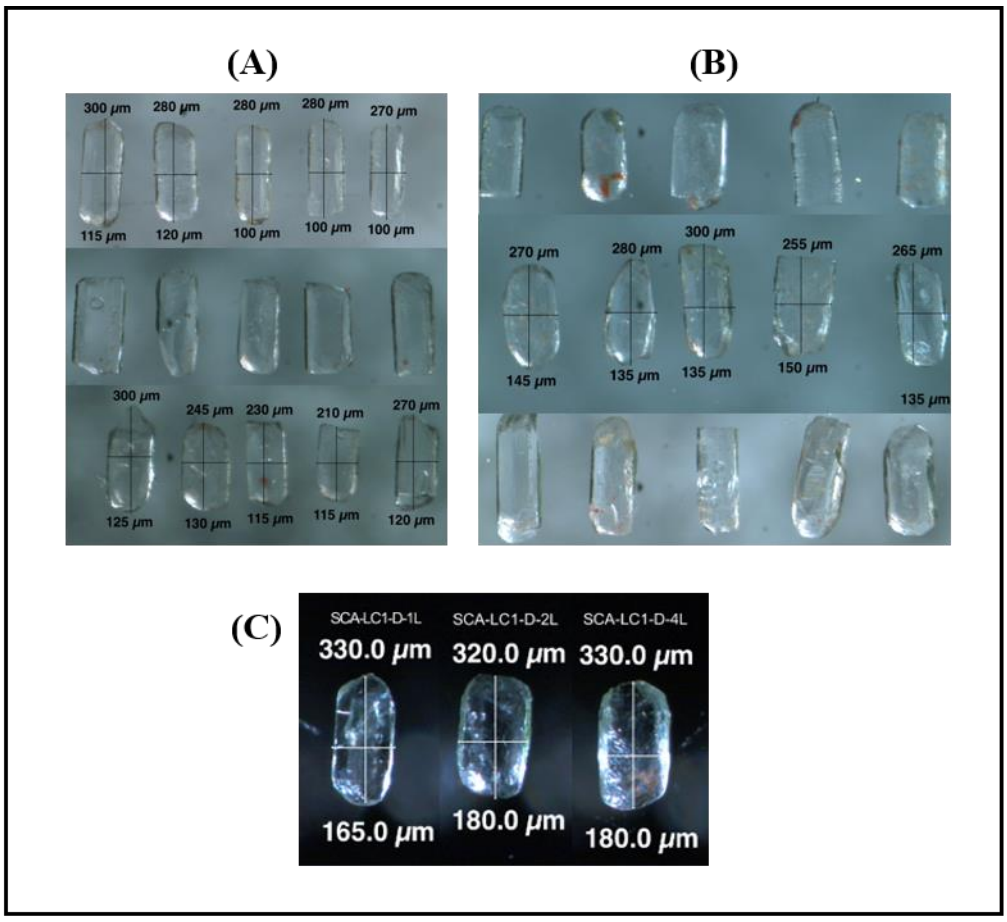

Figure 17: Clast LC1-D (granitic gniess) analyzed grains, (A) MCA-LC1-D1-3 apatite. (B) MCA-LC1-D4-6 apatite. (C) Single grain apatite aliquots: SCA-LC1-D-1, SCA-LC1-D-2, SCA-LC1-D-4.

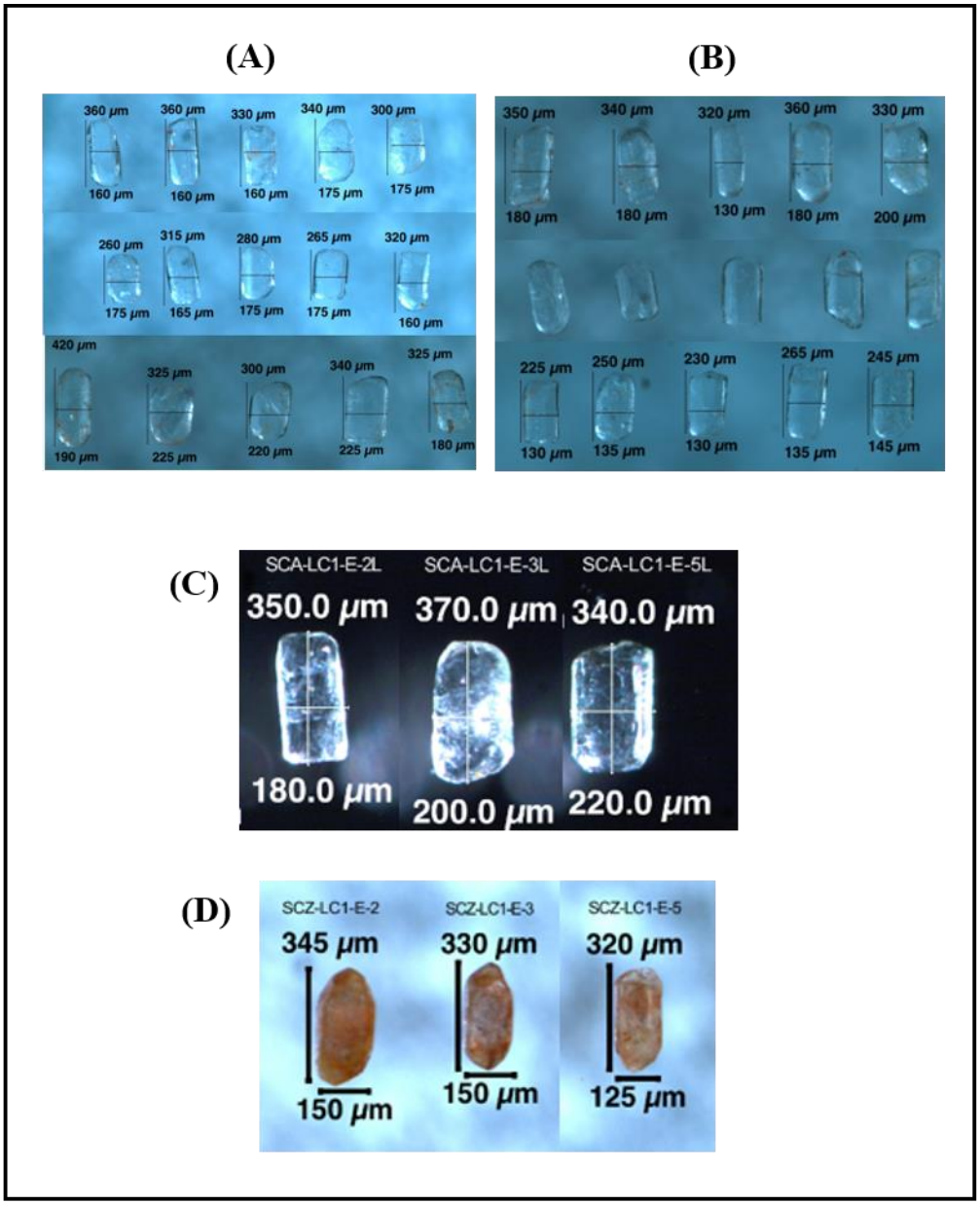

Figure 18: Clast LC1-E (granitic gniess) analyzed grains, (A) MCA-LC1-E1-3 apatite. (B) MCA-LC1-E4-6 apatite. (C) Single grain apatite aliquots: SCA-LC1-E-2, SCA-LC1-E-3, SCA-LC1-E-5 (D) Single grain zircon aliquots: SCZ-LC1-E-2, SCZ-LC1-E-3, SCZ-LC1-E-5.

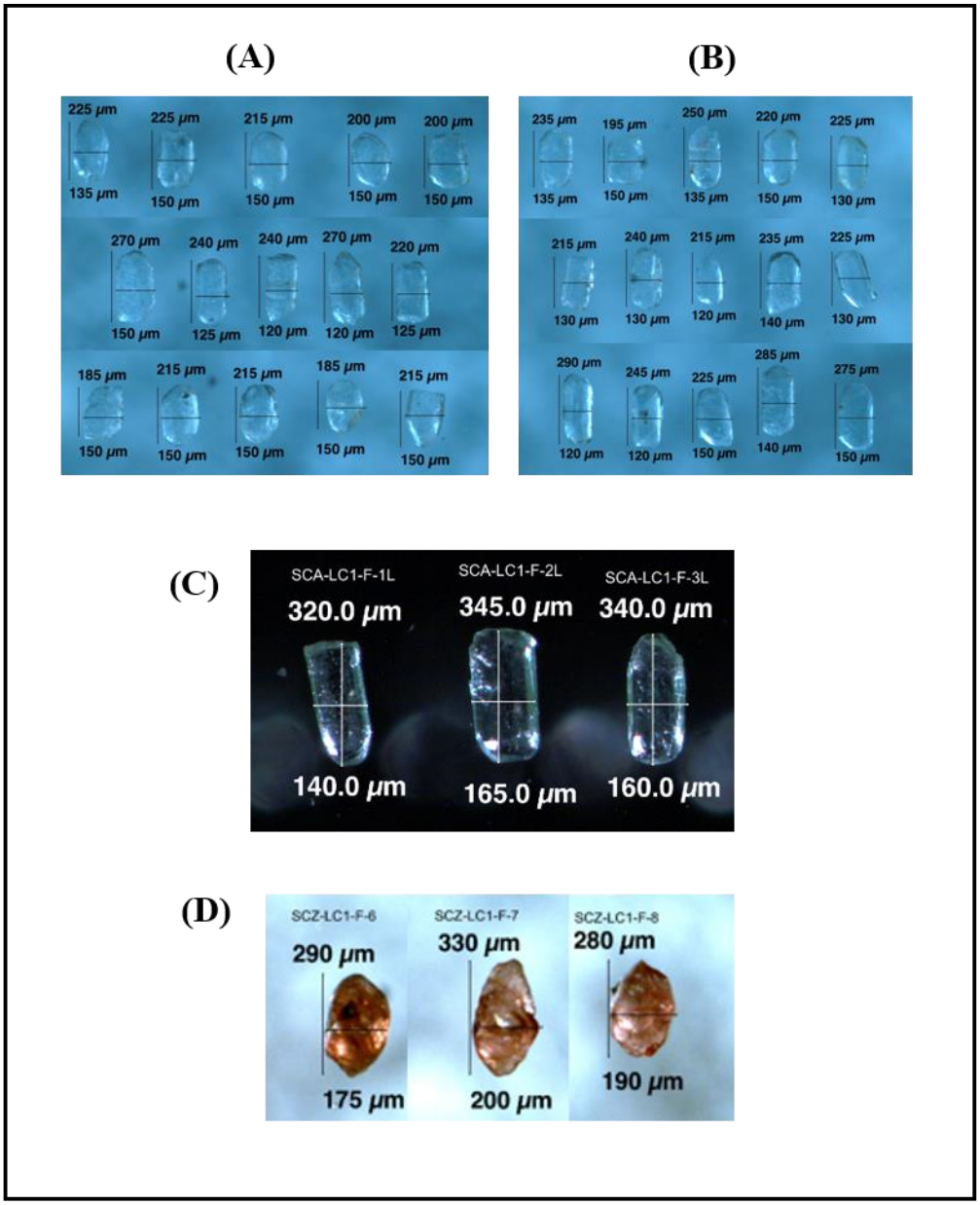

Figure 19: Clast LC1-F (garnet schist) analyzed grains, (A) MCA-LC1-F1-3 apatite. (B) MCA-LC1-F4-6 apatite. (C) Single grain apatite aliquots: SCA-LC1-F-1, SCA-LC1-F-2, SCA-LC1-F-3 (D) Single grain zircon aliquots: SCZ-LC1-F-6, SCZ-LC1-F-7, SCZ-LC1-F-8.

3. Results

Apatite: Two aliquots containing multiple apatite crystals and three aliquots of single-grain apatite crystals from cobbles LC1-B, LC1-C, LC1-D, LC1-E and LC1-F were analyzed (Table 2). Measured aliquot apparent ages are plotted against their respective effective uranium concentration, (eU = [U] + 0.235 [Th]) in (Figures 20, 21 and 22). Apparent ages for all aliquots are also plotted against grain-size represented as equivalent spherical radius (R_s), the radius of a sphere of equal surface area to volume ratio of the mineral calculated from physical grain dimension measurement (Figure 21 and 22; Farley et al. 1996).

Aliquots from LC1-B have a wide apparent age scatter from 29.9 ± 1.2 Ma to 62.1 ± 4.3 Ma. The two multi-crystal aliquots (MCA-LC1-B1-3 and MCA-LC1-B2-4) and one single grain aliquot (SCA-LC1-B-2) have similar ages of 51.7 ± 2.3 Ma, 62.1 ± 4.3 Ma and 60.7 ± 1.6 Ma, respectively. The remaining two single grain aliquots (SCA-LC-B1-3 and SCA-LC1-B-4) report ages similar to each other, 34.7 ± 0.8 Ma and 29.9 ± 1.2 Ma, but are substantially younger than the other three aliquots. Cobble data, plotted apparent age vs. eU (Figure 21), show minor variance in eU between all aliquots and a positive correlation between apparent age and eU. The same data, plotted apparent age vs. grain size, a correlation is absent.

Cobble LC1-C, a granitic gneiss, apparent ages scatter between 87.9 ± 2.9 Ma and 179.2 ± 11.4 Ma. The multiple crystal aliquots have common ages of 177.6 ± 9.6 Ma and 179.2 ± 11.4 Ma and two of the three single grain aliquots (SCA-LC1-C-2 and SCA-LC1-4) have common ages of 87.9 ± 2.9 Ma and 89.9 ± 3.4 Ma. On an apparent age vs.

eU plot (Figure 21) a strong positive correlation shown. When plotted as apparent age vs. grain size a negative correlation is present where apparent age increases as a function of decreasing grain size.

Ages obtained from cobble LC1-D show similar characteristics to samples LC1-B and LC1-B. A large age scatter exists between 88.7 ± 4.8 Ma and 150.4 ± 5.6 Ma and, once more, the multiple crystal aliquots have similar ages of 113.5 ± 4.5 Ma and 112.1 ± 4.8 Ma. The three single crystal ages, however, share no age commonality within, nor with the multiple crystal aliquots. Plotted apparent age vs. eU these data correlate positively; however, a trend when apparent age is plotted against grain size cannot be established.

Apparent ages measured from cobble LC1-E scatter from 85.3 ± 3.2 Ma to 149.2 ± 92 Ma. One multiple crystal aliquot (MCA-LC1-E4-6) and two single-crystal aliquots (SCA-LC1-E-2 and SCA-LC1-E-5) have similar ages of 115 ± 6.6, 107.5 ± 3.6 and 109.5±5 Ma. The remaining multiple crystal apatite is ~30% older and the third single crystal aliquot (SCA-LC1-E-5) is ~30% younger. When apparent age is plotted against eU no trend is observed. Such is the case when plotted apparent age vs. grain size.

Cobble LC1-F aliquots report helium ages between 57.2 ± 3.8 Ma and 64.3 ± 2.1 Ma for four of the five aliquots. The fifth (SCA-LC1-F-3) has an apparent age of 104.1 ± 4.2 Ma. These data plotted apparent age vs. eU show a positive correlation and, to a lesser extent, on a plot of apparent age vs. grain size.

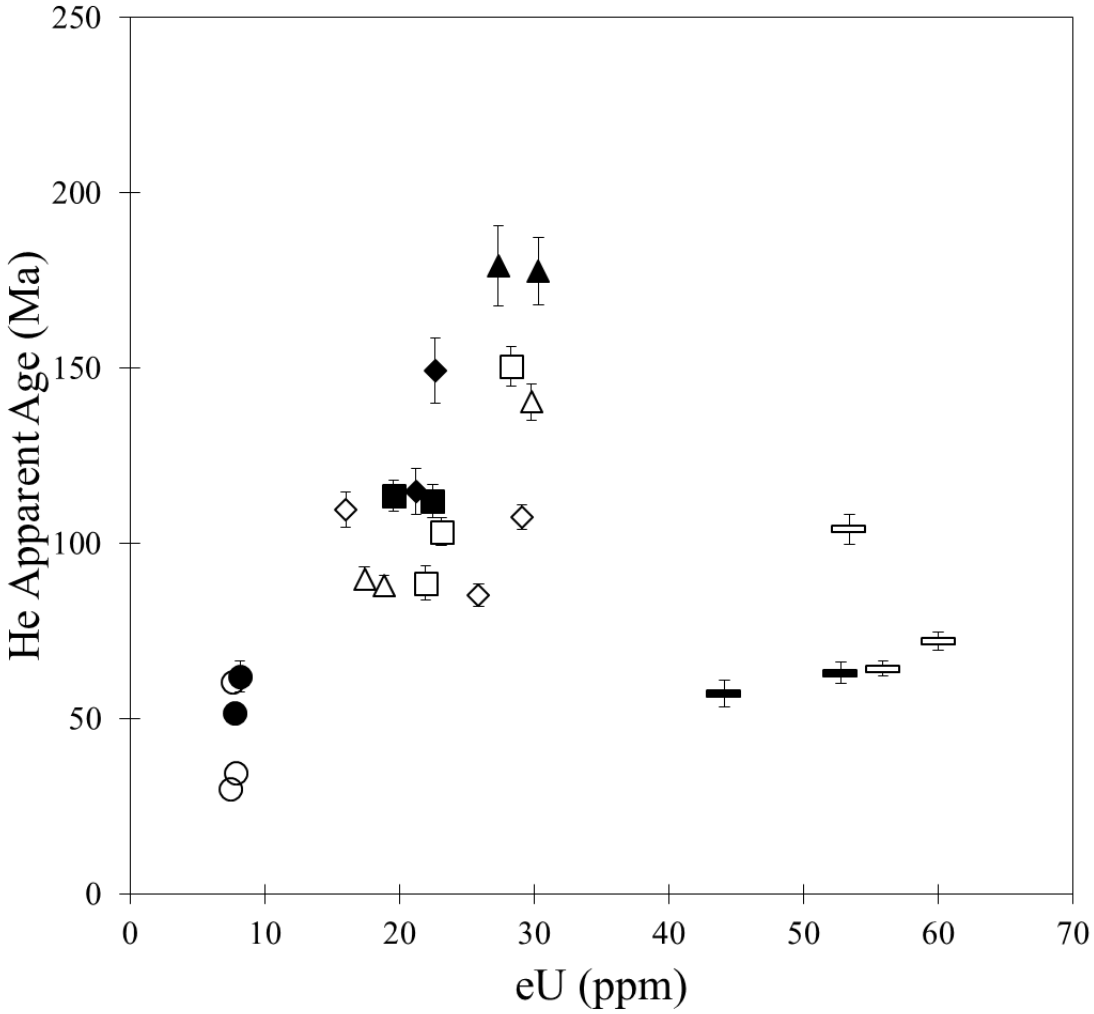

Figure 20: AHe age vs. eU. (circles) cobble LC1-B. (triangles) cobble LC1-C. (squares) Cobble LC1-D. (diamonds) cobble LC1-E. (bars) cobble LC1-F. Closed markers represent multi-crystal aliquots. Open markers represent single crystal aliquots. Error bars are 1σ.

Sample Name	mass (µg)	R_s (µm)	U (ppm)	Th (ppm)	Sm (ppm)	eU (ppm)	Raw age (Ma)	4He (ncc)	Ft	Corr. Age (Ma)	± 1σ (Ma)	# grains
Apatite												
MCA-LC1-B1-3	121.6	70.9	5.4	8.0	94.3	7.8	40.8	4.5	0.79	51.7	2.3	15
MCA-LC1-B4-6	116.7	66.6	5.5	9.3	98.8	8.2	48.1	5.4	0.78	62.1	4.3	15
SCA-LC1-B-2	25.8	110.0	5.3	8.0	87.6	7.6	52.2	1.2	0.86	60.7	1.6	1
SCA-LC1-B-3	29.1	109.8	5.1	9.4	119.9	7.8	29.9	0.8	0.86	34.7	0.8	1
SCA-LC1-B-4	28.8	108.9	5.0	8.5	89.6	7.4	25.7	0.6	0.86	29.9	1.2	1
MCA-LC1-C1-3	146.6	78.1	21.9	32.8	169.2	30.3	143.2	76.6	0.81	177.6	9.6	15
MCA-LC1-C4-6	149.9	78.5	20.4	26.7	141.1	27.3	144.8	71.5	0.81	179.2	11.4	15
SCA-LC1-C-2	24.6	101.3	14.6	16.5	91.2	18.9	74.7	4.2	0.85	87.9	2.9	1
SCA-LC1-C-3	24.2	98.6	23.8	22.8	152.0	29.8	118.8	10.3	0.85	140.4	5.1	1
SCA-LC1-C-4	15.9	108.4	13.5	14.0	125.1	17.4	77.3	2.5	0.86	89.9	3.4	1
MCA-LC1-D1-3	107.5	61.8	17.2	7.9	102.1	19.6	86.7	21.8	0.76	113.5	4.5	15
MCA-LC1-D4-6	119.9	69.0	17.7	18.2	109.5	22.5	87.9	28.4	0.78	112.1	4.8	15
SCA-LC1-D-1	11.4	88.1	20.1	10.6	123.8	23.1	85.8	2.7	0.83	103.3	4.0	1
SCA-LC1-D-2	19.9	94.0	18.3	9.3	309.5	22.0	74.7	3.8	0.84	88.7	4.8	1
SCA-LC1-D-4	13.6	94.6	20.2	32.1	114.4	28.3	126.0	5.9	0.84	150.4	5.6	1
MCA-LC1-E1-3	282.3	94.7	19.6	7.4	280.5	22.7	125.8	94.2	0.84	149.2	9.4	15
MCA-LC1-E4-6	243.8	78.3	18.4	6.8	264.5	21.2	93.4	56.5	0.81	115.0	6.6	15
SCA-LC1-E-2	15.9	95.6	25.4	10.3	265.4	29.1	90.8	5.0	0.84	107.5	3.6	1
SCA-LC1-E-3	22.0	105.2	21.9	12.2	247.5	25.9	73.1	4.9	0.86	85.3	3.2	1
SCA-LC1-E-5	22.5	111.6	14.3	2.5	241.2	16.0	95.0	4.0	0.87	109.5	5.0	1
MCA-LC1-F1-3	107.0	72.0	41.8	7.6	110.4	44.1	45.6	25.9	0.80	57.2	3.8	15
MCA-LC1-F4-6	112.7	70.5	49.5	11.4	122.2	52.8	49.9	35.8	0.79	63.0	3.1	15
SCA-LC1-F-1	12.3	76.4	56.3	12.8	149.7	60.0	58.2	5.2	0.81	72.1	2.7	1
SCA-LC1-F-2	17.7	88.8	51.2	17.8	121.4	55.9	53.5	6.4	0.83	64.3	2.1	1
SCA-LC1-F-3	10.2	86.3	50.8	8.4	137.1	53.4	86.2	5.7	0.83	104.1	4.2	1

Table 2: Results of (U-Th)/He analysis of apatite crystals from clasts LC1-B through LC1-F. SCA=single crystal apatite. MCA=multi-crystal apatite.

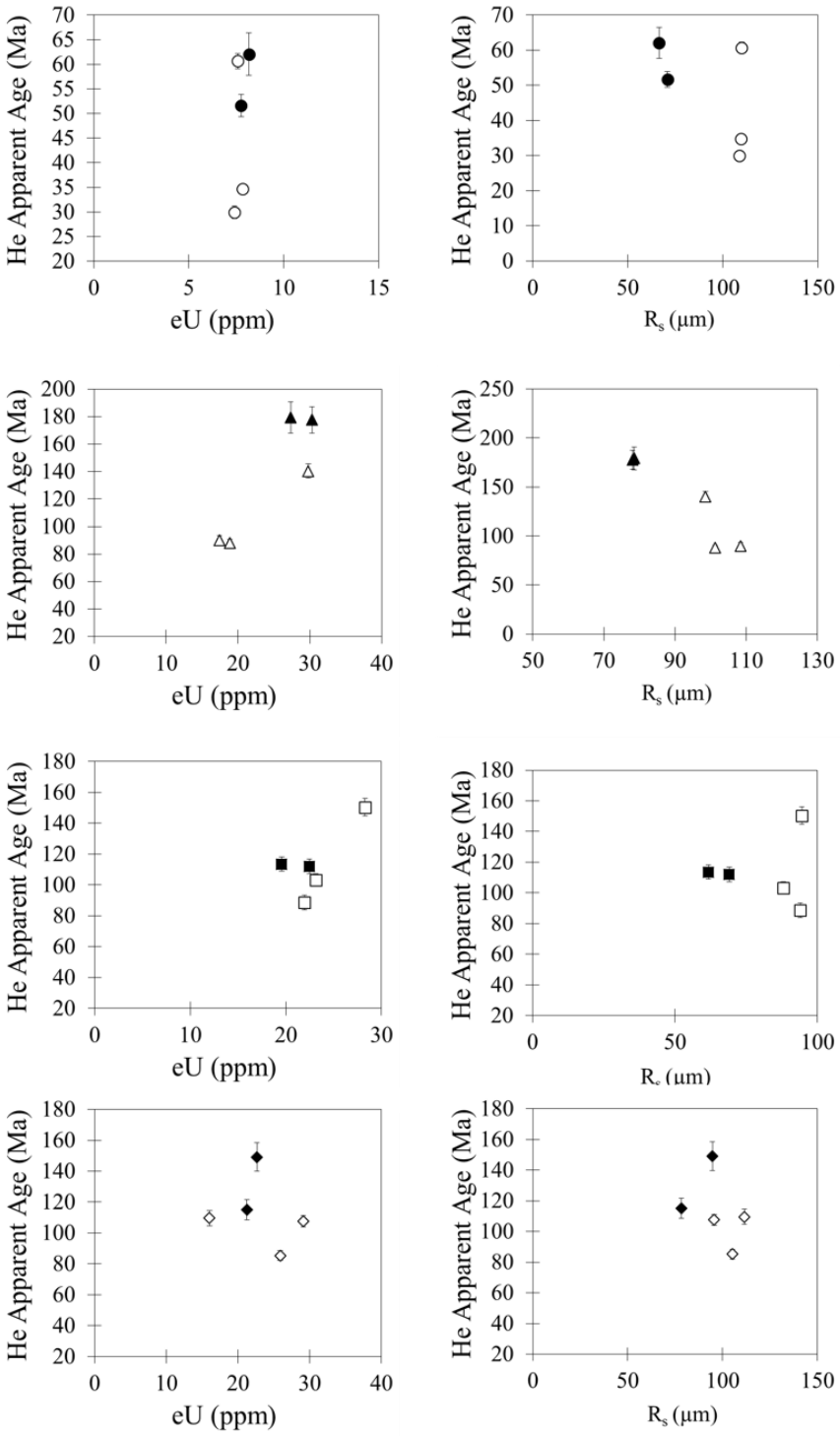

Figure 21: Apparent apatite age vs. eU and apparent apatite age vs. grain size plots for Sample LC1-B (circles), LC1-C (triangles), LC1-D (squares), LC1-E (diamonds). Open Markers represent single grain aliquots. Closed markers represent multiple grain aliquots.

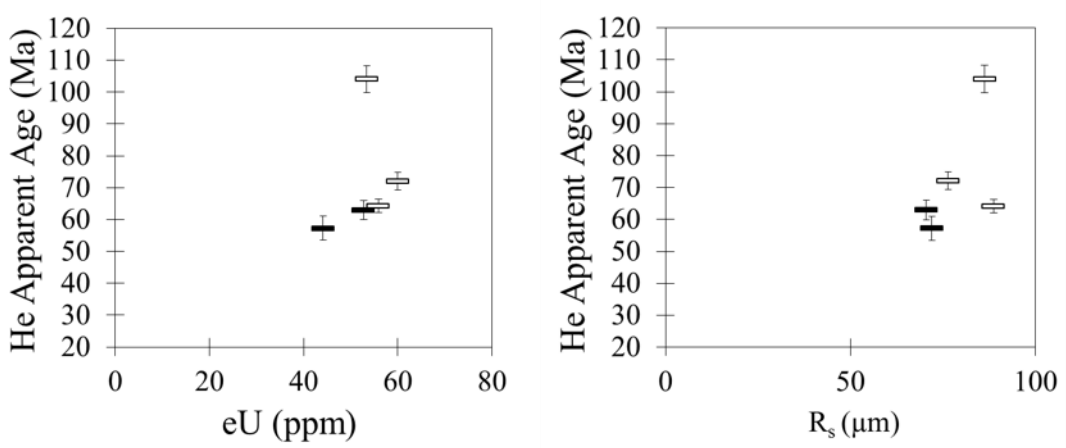

Figure 22: Apparent apatite age vs. eU and apparent apatite age vs. grain size plots for sample LC1-F (bars).Open markers represent single grain aliquots. Closed markers represent multiple grain aliquots.

Zircons: Three single-grain zircon aliquots from samples LC1-B, LC1-C, LC1-E, and LC1-F were analyzed. Results are reported in Figure 23, 24, 25, and Table 3.

Apparent zircon ages determined from cobble LC1-B show similar ages ranging from 103.5 ± 8.5 Ma to 112.9 ± 16.7 Ma. Measured eU between the samples range between 200 ppm and 800 ppm and no correlation with age is visible (Figure 24). Grain-size variance between the aliquots is minimal, thus when plotted against zircon apparent age, no trend is observed.

Data generated from cobble LC1-C show a moderate dispersion of very young apparent ages between 4.9 ± 0.6 Ma and 11.9 ± 1.4 Ma. When apparent age is plotted against eU (Figure 24), we see a positive correlation, where the youngest sample (SCZ-LC1-C-2) contains the lowest concentration of eU and oldest sample (SCZ-LC1-C-5)

contains the highest of the three aliquots. A positive correlation is also observed when these measured ages are plotted against grain size, between 70-86 µm.

Cobble LC1-E zircons yields a narrow scatter of ages ranging between 42.5 ± 6.4 Ma and 50.2 ± 8.2 Ma. No trend is visible when these ages are plotted against eU. On a plot of apparent age vs. grain size however, a positive correlation between the youngest zircon, SCZ-LC1-E-2 and the oldest SCZ-LC1-E-5.

Samples measured from the final cobble, LC1-F, report comparatively old ages to the former three cobbles with the greatest age dispersion and uncertainty between the three aliquots. Ages from these aliquots range from 507.5 ± 72 Ma to as old as 874.7 ± 86.5 Ma. When zircon ages from this cobble are plotted against the aliquots respective concentration of eU, no trend is visible. An observable trend between grain size and the apparent ages of these zircons is also absent.

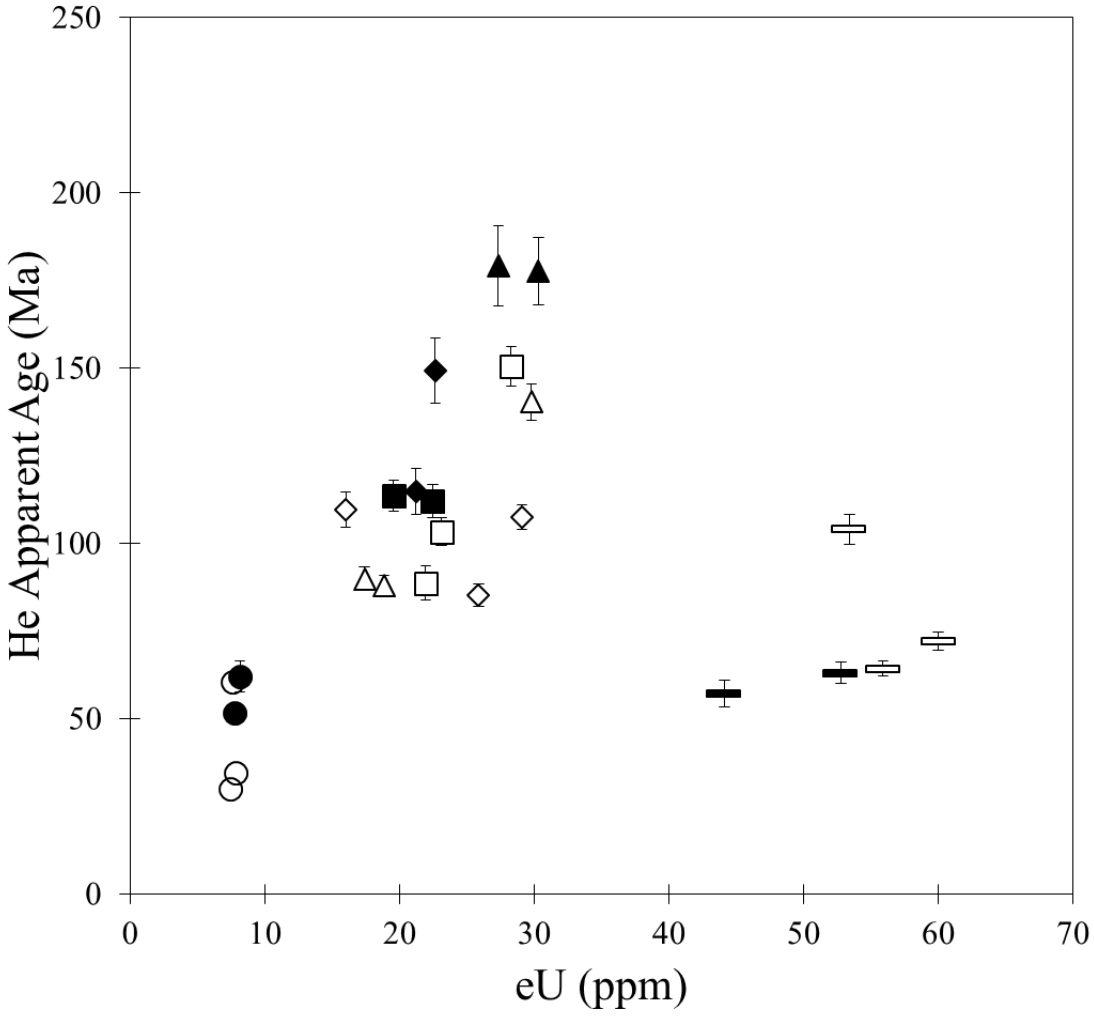

Figure 20: AHe age vs. eU. (circles) cobble LC1-B. (triangles) cobble LC1-C. (squares) Cobble LC1-D. (diamonds) cobble LC1-E. (bars) cobble LC1-F. Closed markers represent multi-crystal aliquots. Open markers represent single crystal aliquots. Error bars are 1σ.

Sample Name	mass (µg)	R_s (µm)	U (ppm)	Th (ppm)	eU (ppm)	Raw age (Ma)	Ft	4He (ncc)	Corr. Age (Ma)	± 1σ (Ma)	# grains
Zircon											
SCZ-LC1-B-4	35.25	115.15	253.09	93.15	274.98	92.00	0.89	108.84	103.47	8.46	1
SCZ-LC1-B-6	34.04	107.20	683.94	141.01	717.08	99.52	0.88	296.25	112.87	16.70	1
SCZ-LC1-B-7	28.64	105.00	209.91	74.11	227.33	94.75	0.88	75.22	107.81	14.49	1
SCZ-LC1-C-2	7.00	68.69	3278.25	1107.32	3538.47	4.00	0.82	12.24	4.89	0.60	1
SCZ-LC1-C-3	7.44	70.71	3915.34	741.80	4089.66	8.15	0.82	30.00	9.89	1.15	1
SCZ-LC1-C-5	8.52	85.28	4130.86	1789.68	4551.44	10.17	0.85	47.74	11.94	1.35	1
SCZ-LC1-E-2	22.87	92.41	5220.42	770.25	5401.43	36.69	0.86	549.46	42.47	6.41	1
SCZ-LC1-E-3	14.93	91.67	4493.16	312.75	4566.66	42.59	0.86	352.12	49.35	7.92	1
SCZ-LC1-E-5	12.03	78.43	2530.79	333.92	2609.26	42.22	0.84	164.35	50.22	8.19	1
SCZ-LC1-F-6	7.34	100.83	502.90	411.95	599.71	442.79	0.87	245.05	507.50	71.97	1
SCZ-LC1-F-7	19.95	115.12	241.91	177.46	283.61	580.67	0.89	628.32	653.84	63.66	1
SCZ-LC1-F-8	16.93	106.40	331.40	411.73	428.16	767.87	0.88	718.69	874.72	86.48	1

Table 3: Results of (U-Th)/He analysis of zircon crystals from clasts, LC1-B, LC1-C, LC1-E, LC1-F

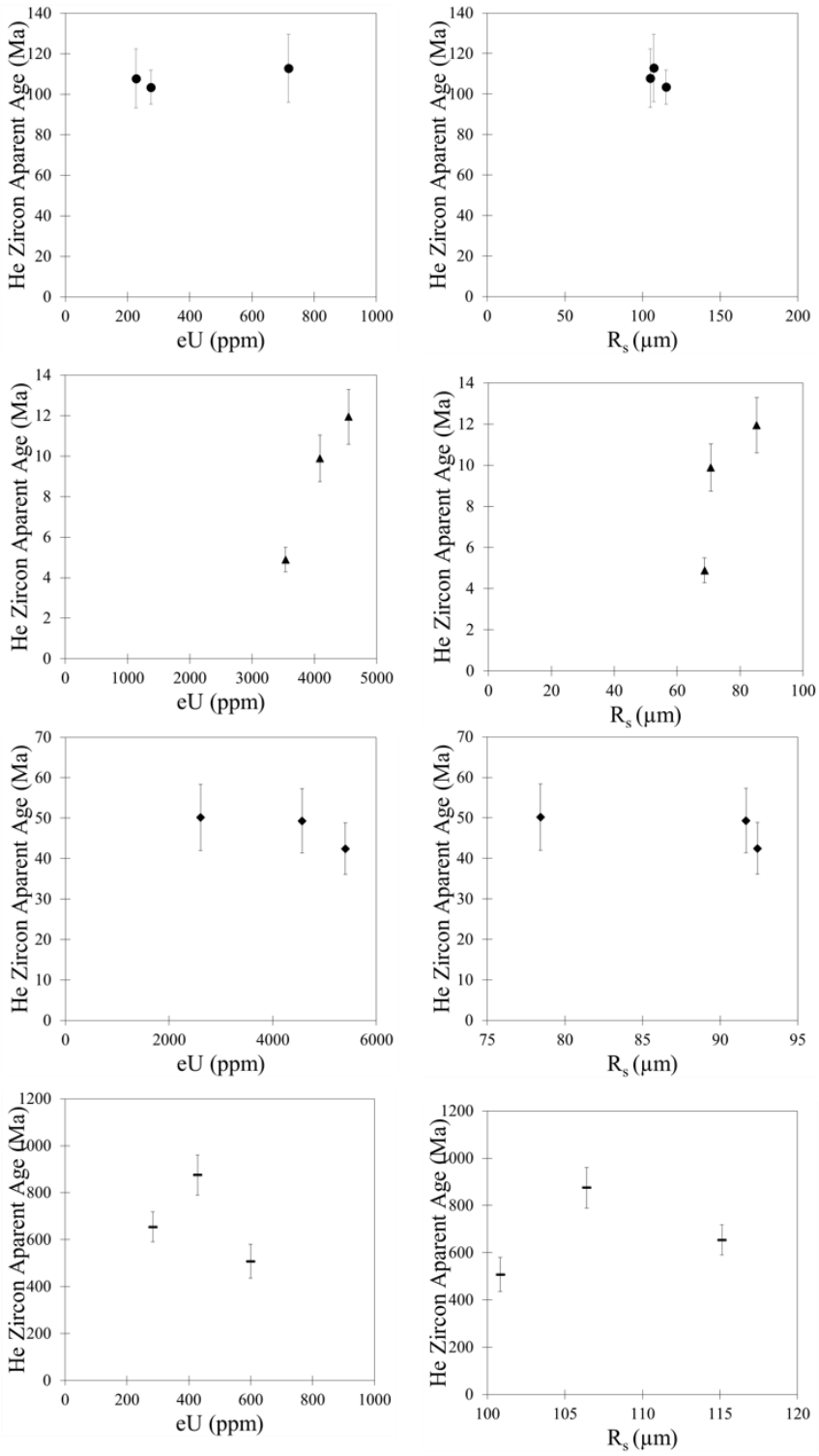

Figure 24: Apparent zircon age vs. eU and apparent zircon age vs. grain size plots for sample LC1-B (circles), LC1-C (triangles), LC1-E (diamonds) and LC1-F (bars). OpenMarkers represent single grain aliquots. Closed markers represent multiple grain aliquots.

Apatite vs. Zircon: To better understand the relationship between apatite apparent ages and zircon apparent ages measured from the same cobble, weighted averages were taken of apatite aliquots and zircon aliquots representing apparent apatite cobble ages and apparent zircon coble ages. When plotted against each other (Figure 25) with a 1:1 trend line, two cobbles LC1-B and LC1-F are observed above the line and represent, on a clast basis, that apatite apparent ages are younger than zircon apparent ages. Samples LC1-C and LC1-E fall below the line where apparent apatite ages are older than apparent zircon ages.

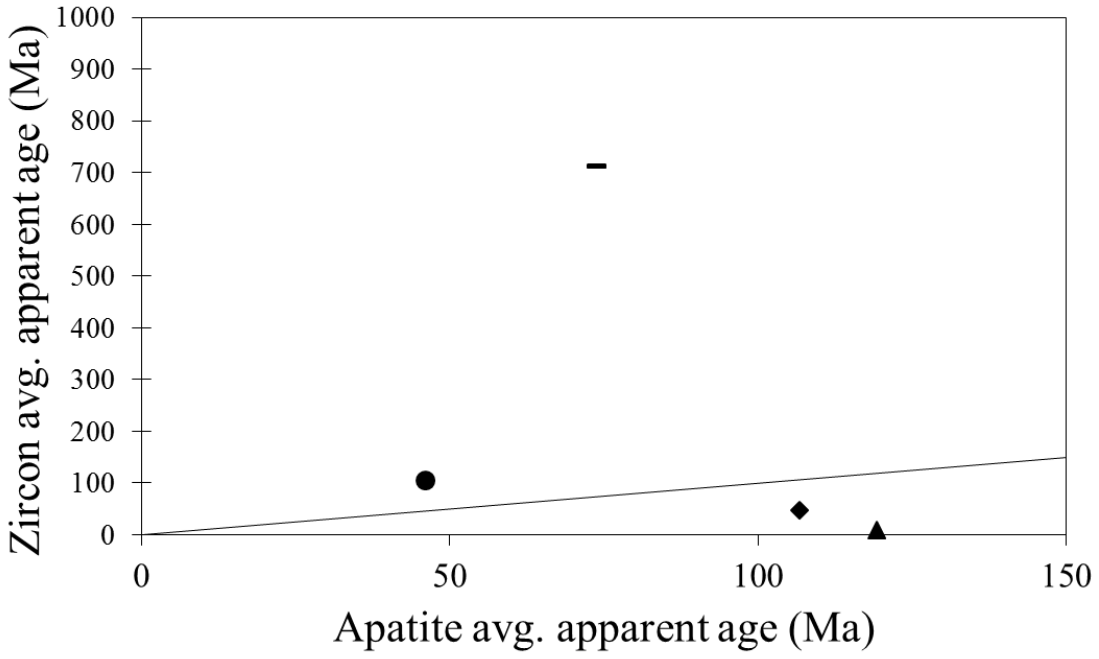

Figure 25: Zircon apparent age vs. Apatite apparent age plot for samples LC1-B (circle), LC1-C (triangle), LC1-E (diamond) and LC1-F (bar) with 1:1 line.

4. Discussion and Conclusions

There are several problematic aspects of the data obtained from this study which must be addressed before a geologic interpretation can be made from them. First of which is the inversion of apatite and zircon apparent ages. It is expected that samples taken from the same rock would show apparent zircon ages older than apparent apatite ages. A zircon from the sample would have spent more time below the closure temperature of ~200°C (Reiners et al., 2001) and therefore, would accumulate more radiogenic helium than an apatite from the same sample, as apatite would not start accumulating helium until it reaches temperatures lower than ~70ºC. However, two of the four cobbles analyzed (LC1-C and LC1-E) show average apparent zircon ages younger than apparent apatite ages (Figure 25). It is my interpretation that this relationship is an artifact of abnormally young zircon apparent ages rather than abnormally old apparent apatite ages. The weighted average of zircon aliquot apparent ages from sample LC1-C is 9.1 ± 0.6 Ma, ~110 Ma younger than the average apparent apatite age of the same clast. Sample LC1-E has an average apparent zircon age of 47.1 ± 4.3 Ma with coincident apatite aliquots averaging to 106.7 ± 2.1 Ma. One potential explanation for the anomalously low apparent zircon ages is a change from a crystalline matrix which impedes ^{4}He mobility to a metamict state which greatly accelerates ^{4}He diffusion as a function of natural radiation damage within old zircons having a long low-temperature thermal history (Hurley, 1954; Nasdala et al., 2004; Reiners et al., 2005). It is important to note that the helium diffusion characteristics of zircon, whether apparent ages are young (Reiners et al. 2004) or old (Nasdala et al. 2004) do not change as long as [U] < ~1000 ppm and that a sharp

decrease in zircon apparent age occurs with increasing uranium concentration above ~1000 ppm (Reiners, 2005). The three single-grain aliquots from sample LC1-C (SCZ-LC1-C-2, SCZ-LC1-C-3, and SCZ-LC1-C-5), have uranium concentrations of 3,278 ppm, 3,915 ppm, and 4,130 ppm, respectively. Sample aliquots from LC1-E (SCZ-LC1-E-2, SCZ-LC1-E-3, and SCZ-LC1-E-5) have similarly high uranium concentrations of 5,220 ppm, 4,493 ppm, and 2,530 ppm. Thus, it is my interpretation that these zircon samples have young ages as a result of natural radiation damage producing lower closure temperatures than "normal" zircons. It is not clear from the data how low the closure temperature has been lowered, but it must be below the nominal lower limit of the apatite helium partial retention zone of ~50ºC.

Another unexpected relationship exists in aliquots SCA-LC1-B-3 and SCA-LC1-B-4 which have apparent ages of 34.7 ± 0.8 Ma and 29.9 ± 1.2 Ma respectively, younger than the generally accepted Upper-Paleocene depositional age of the Beartooth Conglomerate. The remaining three aliquots from this cobble have apparent ages between 51.7 ± 2.3 Ma and 62.1 ± 4.3 Ma. If the common ages of aliquots SCA-LC1-B-2, MCA-LC1-B1-3, and MCA-LC1-B4-6 are taken to be true (a reasonable assumption given the remainder of all aliquots have apparent ages older than ~55 Ma), perhaps the anomalously low ages of the aliquots in question are the product of lower closure temperatures for some unrecognized reason (i.e., processes which lead to a lowering of closure temperature on a grain by grain basis of approximately the same size from the same sample are not described in the literature). That said, all single grain aliquots from the sample have common eU concentrations and grain sizes yet, measured ^{4}He from the

young aliquots are comparatively much lower (0.8 ncc and 0.6 ncc) than the third (1.2 ncc) suggesting the possibility of lower closure temperatures, preferential zoning of U and Th towards the rim of the grains causing young ages as a result of alpha-ejection or, potentially, unaccounted for analytical error.

The remainder of the data obtained from this study are consistent with the depositional age of the Beartooth Conglomerate, that is, all aliquots have apparent ages of ~55 Ma and older. Another observation that must be addressed is scatter of apparent apatite ages within individual clasts. Corrected ages determined from this study have ages spanning over 100 million years. Single-sample apparent apatite age scatter as well as anomalously old apparent apatite ages compared to coincident apatite fission-track data is commonly reported from a variety geologic settings (Crowley et al., 2002, Green et al., 2006; Peyton et al., 2012). Several causes of apparent apatite age scatter are the effect of natural radiation damage on helium diffusion (Shuster et al., 2006; Flowers et al., 2009), the effect of grain size (Reiners and Farley, 2001) and the presence of U- and Th-rich inclusions (House et al. 1997, Vermeesch 2006). Shuster et al. (2006), with the motivation of characterizing the relationship between apatite apparent age and eU concentration as a possible mechanism to describe the occurrence of scattered apparent apatite ages, conducted stepwise degassing diffusion experiments on 39 apatite samples. Results from ther study indicate that the closure temperature of apatite varies from ~50 to 115ºC. Shuster et al. (2006) argue that [^{4}He] is a proxy for natural radiation damage accumulated below the closure temperature and this damage acts to impede the mobility of radiogenic helium in the form of helium "traps" thereby increasing the grains bulk ^{4}He

retentivity, leading to older apparent ages as a function of increasing natural radiation damage and cooling rate. This helium trapping model (HeTM; Figure 26), coupled with a ^{4}He production-diffusion model indicated that the closure temperature of apatite will vary with both cooling rate and with eU concentration (Shuster et al., 2006).

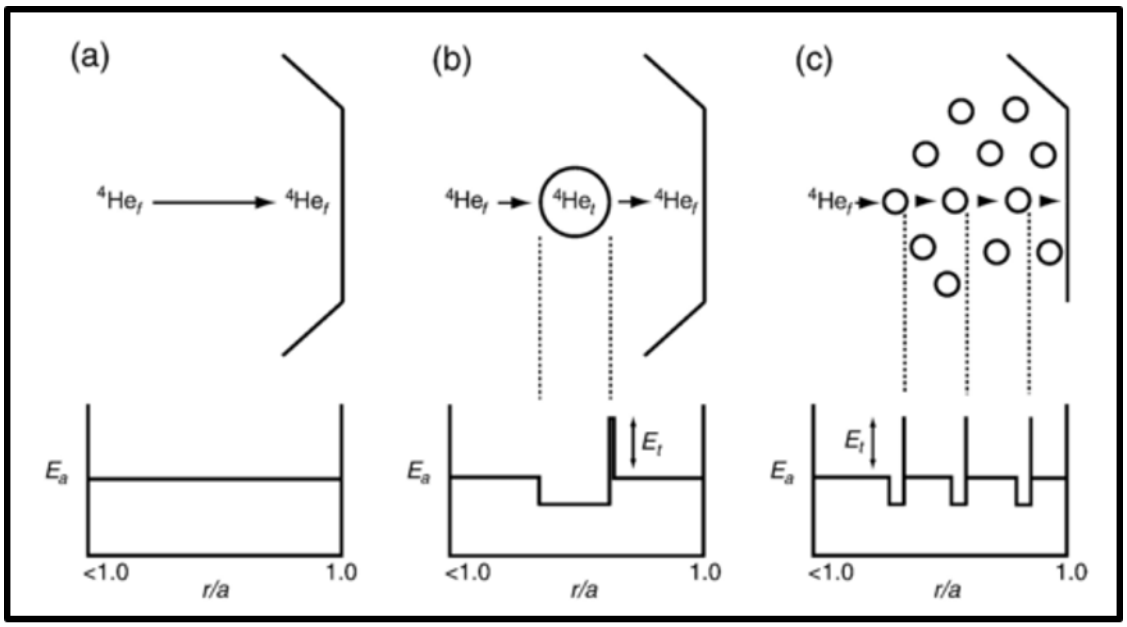

Figure 26: (from Shuster et al., 2006) A schematic model of the potential influence that isolated sites of radiation damage may have on helium diffusion kinetics. (a) Diffusion of a ^{4}He atom across a given distance in a mineral *without* radiation damage. (b) Diffusion of a ^{4}He atom across the same distance in a mineral *with* radiation damage; the circle represents a damage site. (c) The same as (b) after more sites of radiation damage accumulate. The upper panels are cartoons of the crystal with the ^{4}He atom motion due to diffusion indicated by the arrows in the vicinity of the crystal surface. Lower panels are plots of the effective activation energy for diffusion as a function of radial position, r, across a sphere of radius a; $r/a=1$ corresponds to the crystal surface, He_f is a "free" helium atom located within the undamaged crystal structure, He_t is a "trapped" atom located within a site of radiation damage. E_a is the activation energy for volume diffusion through regions of the crystal entirely free of radiation damage and E_t is the energy required of a helium atom to move out of a trap back into the undamaged crystal.

Reiners and Farley (2001) describes the relationship between grainsize and apparent apatite age from a sample suite collected from the Bighorn Mountain Range which demonstrates that larger crystals retain more radiogenic helium than smaller crystals and thus, large crystals will measure older apparent ages than coincident smaller crystals. Vermeesch et al. (2006) suggests that if an inclusion of high [U] and [Th] (e.g., zircon) were present within a measured apatite sample, α-producer concentration may go under reported with respect to radiogenic helium as the methods used to dissolve sample apatite grains are not aggressive enough to dissolve zircon thus, leading to an overestimated apparent apatite age. It is my interpretation that apparent age scatter present within many samples of this study can be explained by one or a combination of these factors coupled with slow cooling i.e., extended periods of time spent in or near the apatite helium partial retention zone.

I interpret, barring the two aliquots with apparent ages younger than conglomerate depositional age, based on the apatite data from sample LC1-B to have approximately the same closure temperature (~65ºC) and cooled through this temperature ~60 Ma. Coupled with zircon apparent ages from sample LC1-B (~100 Ma) it is possible that this sample as a whole experienced slow cooling from ~190ºC to ~65ºC over a period of roughly 40 Ma. Apparent apatite ages obtained from aliquots of sample LC1-C show a bimodal distribution which is interpreted to be linked to eU concentration. Two single-grain samples, SCA-LC1-C-2 and SCA-LC1-C-4, have apparent apatite ages of 87.9 ± 2.9 Ma and 89.9 ± 3.4 Ma, respectively and eU concentration of 18.9 ppm and 17.4 ppm. The remaining three aliquots have apparent ages of >140 Ma. Effective uranium

concentrations of these samples are 28 ppm and higher. The positive correlation between apparent apatite age and eU can be seen in Figure 21. I interpret the bimodal distribution of apatite data obtained from clast LC1-C, and the observable dependence on eU concentration, to be the result of natural radiation damage. There is, however, another relationship observed whereby the multiple crystal aliquots from the sample (smaller in grain-size) have some of the oldest ages. This is at odds with the finding of Reiners and Farley (2001). One possibility allowing these smaller grained multiple crystal aliquots to have older apparent ages is the presence of U- and Th-rich inclusions (House et al., 1997, Vermeesch, 2006) despite the fact that great care was taken to select only the most pristine apatites for age determination. Smaller than observable U- and Th- rich inclusions may be interpreted to have little effect on the bulk producer concentration however, multiple grain aliquots from this study contained 15 individual apatite grains thus, the probability of measuring grains containing inclusions increases. I interpret these clasts to have spent ~100 Ma cooling slowly through each apatite's respective helium partial retention zone prior to the onset of rapid uplift of the Beartooth Plateau. Aliquots from sample LC1-D and LC1-F, also show a positive correlation between eU concentration and apparent age and are interpreted to demonstrate the influence of natural radiation damage on closure temperature and that slow cooling though variable closure temperatures is responsible for the scatter in ages within each sample. Shuster et al., (2006) suggest that the closure temperature in apatite can range from ~50 to ~115ºC (Figure 27) as a function of cooling rate and eU concentration. It is also suggested even a small variance in eU concentration between intra-clast apatites, such is the case in the samples measured in this study, can change the closure temperature of an apatite by

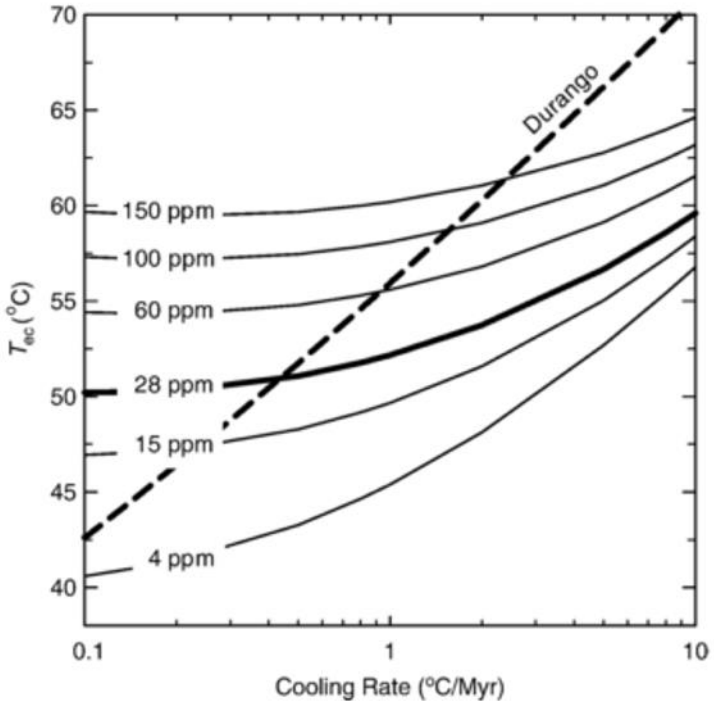

Figure 27: (from Shuster et al., 2006) Effective closure temperature as a function of cooling rate and eU (labeled in ppm) computed from the trapping diffusion model embedded in a ^{4}He production-diffusion model. Results for conventional Durango apatite kinetics are also shown. Simulated cooling paths began at 100ºC at various times selected to yield the reported cooling rates.

~5ºC. Thus, I interpret radiation damage to be the leading cause of age scatter. However, the contributions of radiation damage, grain size effects and possible uranium and thorium rich inclusions do not explain all apparent age scatter within samples suggesting another cause, perhaps U and Th zonation, or analytical error.

Based on the data measured from samples LC1-C, LC1-D, LC1-E, LC1-F, and the apatite data from LC1-B, it is my interpretation that these samples resided within ~4 km of a column of presently eroded basement, an additional ~1 km of basement used in the

hypotheses of Omar et al. (1994), in middle Cambrian time and was never buried deeper than ~3-4 km. The maximum burial depth being obtained in the late Jurassic-early Paleocene just before the onset of rapid uplift of the Beartooth Plateau. During the period of Phanerozoic burial, I suggest that each clast underwent slow cooling in or near the apatite partial retention zone, prior to uplift initiation ~60 Ma. Forward and Inverse modelling using HeFTy (Ketcham, 2005) demonstrate that the above thermal history on an aliquot by aliquot basis, seems plausible (Figure 28). However, when multiple aliquots from the same sample with a large scatter of apparent ages are modeled, no good paths are established. I attribute this to the inability of the software to resolve the presence of multiple closure temperatures within clasts and therefore does not preclude the suggested thermal history. Further, the thermal history can also be resolved by HeFTy when apatite apparent ages and zircon apparent ages from sample LC1-F are used as inputs (Figure 28). However, modelling in HeFTy cannot resolve apparent apatite ages with apparent zircon ages (~100 Ma) measured from sample LC1-B.

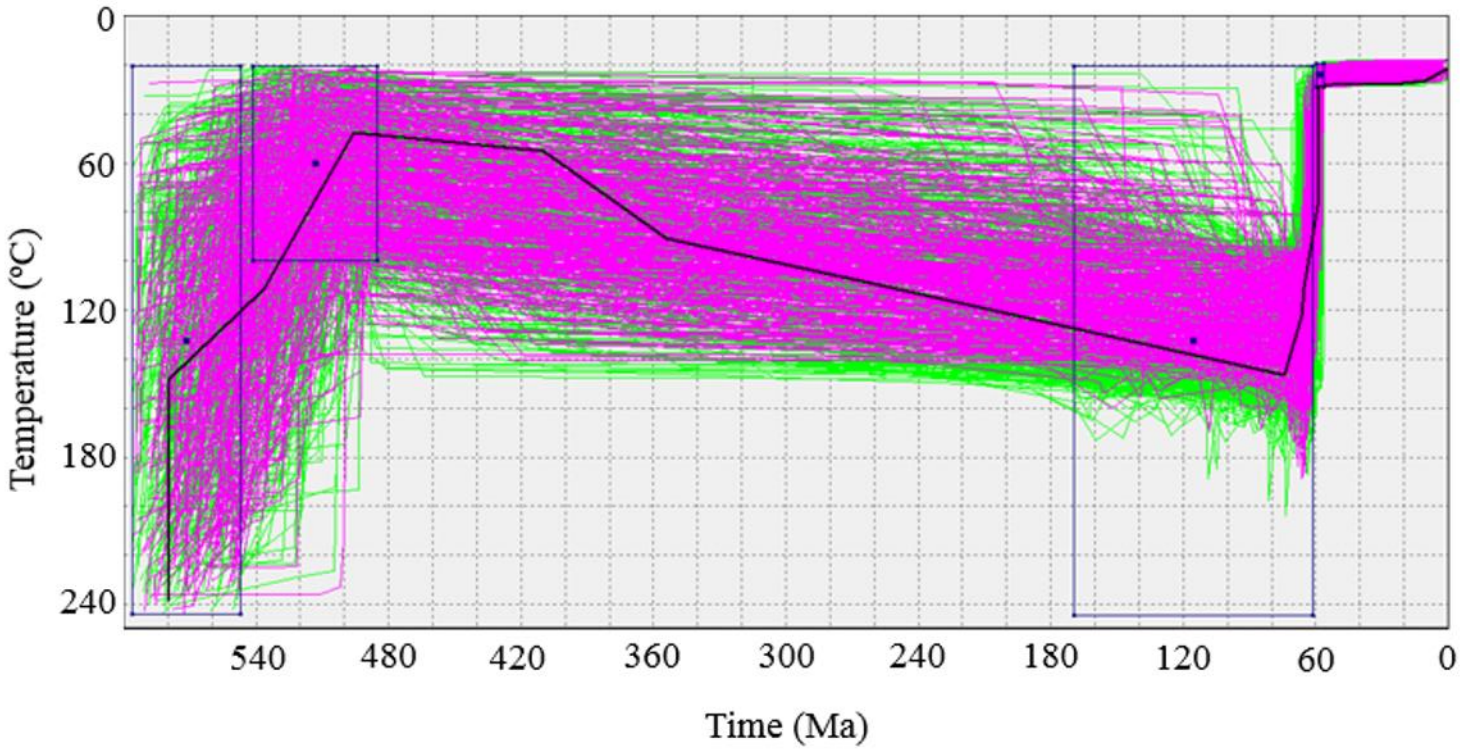

Figure 28: HeFTy model demonstrating the resolvability of a thermal history constrained by 1) the samples resided within the first ~4 km during the Cambrian and 2) were at the surface by the Late Paleocene. Pictured input data are from sample LC1-F apatites and zircons.

From this study I conclude the amount of basement overburden (~3-4 km) used in the hypotheses of Omar et al., (1994) is supported by apparent apatite and zircon ages measured from clasts within the Beartooth Conglomerate. Further, results presented in this study are consistent with the late-Paleocene depositional age designation of the Beartooth Conglomerate i.e., all measured apatite aliquots, with the exception of two, have ages ~55 Ma and older. These data indicate subdued tectonism since the Cambrian, when present-day eroded basement of the Beartooth Range was at or near the surface prior to Paleozoic sedimentation. Burial continued throughout the Mesozoic just prior to uplift, erosion and deposition during the late-Paleocene.

5. References

Bird, P., 1998, Kinematic history of the Laramide Orogeny in latitudes 35°-49°N, western United States: Tectonics, v. 17, n. 5, p. 780-801.

Blackstone, D.L., 1986, Structural geology-Northwest margin, Bighorn Basin: Park County, Wyoming and Carbon County, Montana: Yellowstone-Bighorn Research Association, Field Conference, Guidebook, p.125-135.

Crowley, P.D., Reiners, P.W., Reuter, J.M., and Kaye, G.D., 2002, Laramide exhumation of the Bighorn Mountains, Wyoming: An apatite (U-Th)/He thermochronology study: Geology, v.30, n. 1, p. 27-30.

Coney, P.J., and Reynolds, S.J., 1977, Cordilleran Benioff zones: Nature, v.270, p.403-406.

DeCelles, P.G., 2004, Late Jurassic to Eocene evolution of the Cordilleran thrust belt and foreland basin system, western U.S.A.: American Journal of Science, v. 304, n. 2, p.105-168.

DeCelles, P.G., Gray, M.B., Ridgway, K.D., Cole, R.B., Pivnik, D.A., Pequera, N., and Srivastava, P., 1991a, Controls on synorogenic alluvial fan architecture, Beartooth Conglomerate (Paleocene), Wyoming and Montana: Sedimentology, v. 38, n.4, p. 567-590.

DeCelles, P.G., Gray, M.B., Ridgway, K.D., Cole, R.B., Srivastava, P., Pequera, N., and Pivnik, D.A., 1991b, Kinematic history of a foreland uplift from Paleocene synorogenic conglomerates, Beartooth Range, Wyoming and Montana: Geological Society of America Bulletin, v. 103, p. 1458 – 1475.

Dickinson, W.R., and Snyder, W.S., 1978, Plate tectonics of the Laramide Orogeny, *in* Matthews, V., ed., Laramide folding associated with basement block faulting in the western United States: Geological Society of America Memoir, v. 151, p. 355-366.

Dutcher, L.A.F., Jobling, J.L., and Dutcher, R.R., 1986, Stratigraphy, sedimentology and structural geology of Laramide synorogenic sediments marginal to the Beartooth Mountains, Montana and Wyoming, *in* Garrison, P.B., ed., Geology of the Beartooth uplift and adjacent basins: Montana Geological Society and Yellowstone-Bighorn Research Association Joint Field Conference and Symposium, p. 33-52.

Farley, K.A., 2002, (U-Th)/He data: Techniques, calibrations, and applications, *in* Porcelli, D., Ballentine, C.J., and Wieler, R., eds., Noble gases in geochemistry and cosmochemistry: Review in Mineralogy and Cosmochemistry, v. 47, p. 819-843.

Farley, K.A., Wolf, R.A., and Silver, L.T., 1996, The effects of long alpha stopping distances on (U-Th)/He ages: Geochemica et Cosmochimica Acta, v. 60, n. 21 p. 4223-4229.

Flowers, R.M., Ketcham, R.A., Shuster, D.L., and Farley, K.A., 2009, Apatite (U-Th)/He thermochronometry using a radiation damage accumulation and annealing model: Geochemica et Cosmochimica Acta, v. 73, n.8, p. 2347-2365.

Flueckinger, L.A., 1970, Stratigraphy, petrography, and origin of Tertiary sediments off the front of the Beartooth, Montana-Wyoming [Ph. D. thesis] University Park, Pennsylvania, Pennsylvania State University, 249 p.

Foose, R.M., Wise, D.U., and Garbarini, G.S., 1961, Structural geology of the Beartooth Mountains, Montana and Wyoming: Geological Society of America of America Bulletin, v. 72, p. 1143 – 1172.

Green, P.F., Crowhurst, P.V., Duddy, I.R., Japsen, P., and Holford, S.P., 2006, Conflicting (U-Th)/He and fission track ages in apatite: Enhanced He retention, not anomalous annealing behavior: Earth and Planetary Science Letters, v. 250 n. 3-4, p. 407-427.

Hickey, L.J., 1980, Paleocene stratigraphy and flora of the Clark's Fork Basin, *In* Gingerich, P.D., ed., Early Cenozoic paleontology and stratigraphy of the Bighorn Basin, Wyoming: University of Michigan Papers on Paleontology Number 24, p. 33-49.

House, M.A., Wernicke, B.P., Farley, K.A., and Dumitru, T.A., 1997, Cenozoic thermal evolution of the central Sierra Nevada, California, from (U-Th)/He thermochronometry: Earth and Planetary Science Letters, v. 151, n. 3-4, p.167-179.

Hurley, P.M., 1954, The helium age method and the distribution and migration of helium in rocks. *In* Faul, H., ed., Nuclear Geology: Wiley, New York p. 301-329.

Jobling, J.L., 1974, Stratigraphy, petrology, and structure of the Laramide (Paleocene) sediments marginal to the Beartooth Mountains, Montana [Ph. D. thesis] University Park, Pennsylvania, Pennsylvania State University, 102 p.

Ketcham, R.A., 2005, Forward and inverse modelling of low-temperature thermochronometry data: Reviews in Mineralogy and Geochemistry, v. 58, p.275-314.

Naeser, C.W., 1979, Fission-track dating and geologic annealing of fission tracks, *in* Jager, E., and Hunziker, J.C., eds., Lectures in Isotope Geology: Berlin, Germany, Springer-Verlag p. 154 – 169.

Nasdala, L., Reiners, P.W., Garver, J.I., Kennedy, A.K., Stern, R.A., Balan, E., and Wirth, R., 2004, Incomplete retention of radiation damage in zircon from Sri Lanka: American Mineralogist, v.89, p. 219-231.

Omar, G.I., Lutz, T.M., and Giegengack, R., apatite fission-track evidence for Laramide and post-Laramide uplift and anomalous thermal regime at the Beartooth overthrust, Montana-Wyoming: Geological Society of America Bulletin, v. 106, p. 74-85.

Peyton, S.L., Reiners, P.W., Carrapa, B., and DeCelles, P.B., 2012, Low-temperature thermochronology of the northern Rocky Mountains, western U.S.A.: American Journal of Science, v.312, n. 2., p. 145-212.

Reiners, P.W., Farley, K.A., and Hickes, H.J., 2001, He diffusion and (U-Th)/He thermochronometry of zircon: initial results from Fish Canyon Tuff and Gold Butte: Tectonophysics, n. 349 p. 297-308.

Reiners, P.W., and Farley, K.A., 2001, Influence of crystal size on apatite (U-Th)/He thermochronology: an example from the Bighorn Mountains, Wyoming: Earth and Planetary Science Letters, v.188, n.3-4, p. 413-420.

Reiners, P.W., Spell, T.L., Nicolescu, S., and Zanetti, K.A., 2004, Zircon (U-Th)/He thermochronometry: He diffusion and comparisons with 40Ar/39Ar dating: Geochimica et Cosmochimica Acta, v. 68, n. 8, p. 1857-1887.

Reiners, P.W., Campbell, I.H., Nicolescu, S., Allen, C.M., Hourigan, J.K., Garver, J.I., Mattinson, J.M., and Cowan, D.S., 2005, (U-Th)/(He-Pb) Double dating of detrital zircons: American Journal of Science, v. 305, n. 4, p.259-311.

Saleeby. J., 2003, Segmentation of the Laramide slab-evidence from the southern Sierra Nevada region: Geological Society of America Bulletin, v. 115, n. 6, p. 655-668.

Shuster, D.L., and Farley, K.A., 2003, 4He/3He thermochronometry: Earth and Planetary Science Letters, v.217, n. 10, p. 1-17.

Shuster, D.L., Flowers, R.M., and Farley, K.A., 2006, The influence of natural radiation damage on helium diffusion kinetics in apatite: Earth and Planetary Science Letters, v. 249, n. 3-4 p.148-161.

Spiegel, C., Kohn, B., Belton, D., Berner, Z., and Gleadow, A., 2009, (U-Th-Sm)/He thermochronology of rapidly cooled samples: The effect of Helium implantation: Earth and Planetary Sciences Letters, v. 285, n.1-2 p. 105-114.

Vermeesch, P., Seward, D., Latkoczy, C., Wipf, M., Gunther, D., and Baur, H., 2007, α-emitting mineral inclusions in apatite, their effect on (U-Th)/He ages, and how to reduce it: Geochimica et Cosmochimica Acta, v.71 n. 7, p. 1737-1746.

Wolf, R.A., Farley, K.A., and Silver, L.T., 1996, Helium diffusion and low-temperature thermochronometry of apatite: Geochimica et Cosmochimica Acta, v. 60, n. 21, p. 4231-4240.

Wise, D. U., 1983, Overprinting of Laramide structural grains in the Clark's Fork Canyon are and eastern Beartooth Mountains of Wyoming: Wyoming Geological Association, Annual Field Conference, 34th, Guidebook, p.77-87.